Dynamic correlations in stochastic rotation dynamics

E. Tuzel,[1,2] T. Ihle,[3] and D.M. Kroll[3]

[1]School of Physics and Astronomy, University of Minnesota,
116 Church Street SE, Minneapolis, MN 55455
[2]Supercomputing Institute, University of Minnesota,
599 Walter Library, 117 Pleasant Street S.E.,
Minneapolis, MN 55455
[3]Department of Physics, North Dakota State University, Fargo, ND 58105

The dynamic structure factor, vorticity and entropy density dynamic correlation functions are measured for Stochastic Rotation Dynamics (SRD), a particle based algorithm for fluctuating fluids. This allows us to obtain unbiased values for the longitudinal transport coefficients such as thermal diffusivity and bulk viscosity. The results are in good agreement with earlier numerical and theoretical results, and it is shown for the first time that the bulk viscosity is indeed zero for this algorithm. In addition, corrections to the self-diffusion coefficient and shear viscosity arising from the breakdown of the molecular chaos approximation at small mean free paths are analyzed. In addition to deriving the form of the leading correlation corrections to these transport coefficients, the probabilities that two and three particles remain collision partners for consecutive time steps are derived analytically in the limit of small mean free path. The results of this paper verify that we have an excellent understanding of the SRD algorithm at the kinetic level and that analytic expressions for the transport coefficients derived elsewhere do indeed provide a very accurate description of the SRD fluid.

PACS number(s): 47.11.+j, 05.40.-a, 02.70.Ns

I. INTRODUCTION

Several years ago, Malevanets and Kapral [1, 2] derived a simple and appealing algorithm — often called Stochastic Rotation Dynamics (SRD) or Multi-Particle Collision Dynamics (MPCD) — for the mesoscale modeling of fluctuating fluids. SRD is a particle based simulation technique with simple discrete time dynamics consisting of consecutive streaming and collision steps. It shares many features with Bird's Direct Simulation Monte Carlo (DSMC) algorithm [3], but uses more efficient multi-particle collisions to exchange momentum between the particles. Since there is a Boltzmann H-theorem for the SRD algorithm, and the particle number, momentum, and energy are locally conserved, the correct hydrodynamic behavior is guaranteed at large length and time scales. The algorithm therefore provides a convenient computational tool for solving the underlying thermo-hydrodynamic equations by providing a "hydrodynamic heat bath" which incorporates thermal fluctuations and provides the correct hydrodynamic interactions between embedded particles or polymers. An important advantage of SRD is that its simplified dynamics has enabled the analytical calculation of the transport coefficients and made it possible to obtain a rather complete theoretical understanding of the time-dependent correlation functions, the relaxation to equilibrium [4, 5], and the behavior in shear flow, including shear thinning at high shear rates [6]. Because the algorithm correctly includes long-ranged hydrodynamic interactions and Brownian fluctuations — both of which are generally required for a proper statistical treatment of the dynamics of mesoscopic suspended particles — it has been used to study the behavior of polymers [7, 8, 9], colloids [10, 11], including sedimentation [12, 13, 14], and vesicles in flow [15, 16].

In its original form [1, 2], the SRD algorithm was not Galilean invariant at low temperatures, where the mean free path, λ, is smaller than the cell size a. However, it was shown [4, 17] that Galilean invariance can be restored by introducing a random shift of the computational grid before every collision. In addition to restoring Galilean invariance, this grid shifting procedure accelerates momentum transfer between cells and leads to a collisional contribution to the transport coefficients. Two approaches have been used to analyze the resulting algorithm and determine the shear viscosity and thermal diffusivity. In Refs. [5] and [18], a non-equilibrium kinetic approach is used to derive the transport coefficients. In Refs. [4, 17], a discrete-time projection operator technique was utilized to obtain Green-Kubo relations for the model's transport coefficients, and explicit expressions for the transport coefficients were derived in accompanying papers [19, 20, 21, 22]. The two approaches are complementary and, for the most part, agree in their conclusions. The first is rather straightforward and intuitively appealing, but makes several assumptions which are not easily verified. The projection operator approach justifies in detail several assumptions used in the non-equilibrium calculations of Refs. [5] and [18]; it can also be used to analyze the transport coefficients of the longitudinal modes, namely the bulk viscosity and thermal diffusivity, which are hard to calculate analytically in the non-equilibrium approach [5]. Note, in particular, that the collisional contribution to the thermal conductivity has

not yet been determined using the non-equilibrium methods.

In spite of some claims to the contrary [5], both approaches yield the same results for the transport coefficients. Table I contains a summary of both the collisional and kinetic contributions to the transport coefficients, including references to the original source of the results; the table caption also provides a brief synapsis of some misprints in published articles which may lead to confusion. Simulation results have generally been in good agreement with these predictions. This is particularly true for the shear viscosity, where the results of equilibrium measurements of vorticity fluctuations [4, 17] and the Green-Kubo relations [19, 20] are in excellent agreement with non-equilibrium measurements in shear [5, 18] and Poiseuille [23] flow. The situation with the transport coefficients of the longitudinal modes, namely the bulk viscosity and thermal diffusivity, is somewhat less clear. The only reliable measurements of the thermal diffusivity have entailed equilibrium measurements of the corresponding Green-Kubo relation [19, 20, 21, 22] and a non-equilibrium measurement obtained by setting up a temperature gradient and measuring the resulting energy flux in a regime where the collisional contribution is negligible [5]. To our knowledge, there has been no direct verification of the prediction that the bulk viscosity is zero for SRD.

In this paper we take an alternative approach based on an analysis of the equilibrium fluctuations of the hydrodynamic modes to directly measure the shear and bulk viscosities and thermal diffusivity. Starting with an analysis of vorticity fluctuations to determine the shear viscosity, measurements of the dynamic structure factor are then used to deduce the values of the speed of sound, the thermal diffusivity, and the bulk viscosity. Measurements of the temporal behavior of the entropy correlations are also used to obtain a direct independent measurement of the thermal diffusivity. To our knowledge, this is the first quantitative measurement of the dynamic structure factor for SRD. An earlier measurement by Inoue et al. [24] lead to unphysical results in the large frequency limit, and could not be used to determine the transport coefficients.

The results of these measurements verify directly that the bulk viscosity is indeed zero for this algorithm. In addition, in agreement with earlier work [5, 17, 18, 19, 20, 21], results for the shear viscosity and the thermal diffusivity are in excellent agreement with the theoretical predictions presented in Table I for a wide range of particle densities and mean free paths. However, as noted originally in Ref. [19], and discussed in more detail in Ref. [21], correlations between particles occupying the same collision cell at different time steps lead to an enhanced kinetic contribution to the transport coefficients. This breakdown of the molecular chaos approximation becomes pronounced at small mean free path, λ, since particles do not travel far between collisions and tend to repeatedly have the same collision partners. For most transport coefficients, this additional contribution to the transport coefficients is masked by the collisional contribution, which dominates in the small mean free path regime. The effect is particularly pronounced, however, for the self-diffusion coefficient, for which there is no collisional contribution. Indeed, Ripoll et al. [25, 26] have observed that the self diffusion coefficient is significantly larger than the theoretical prediction of Ref. [17, 20] for small λ/a. Ripoll et al. provided a semi-analytical description of this behavior in which they determined numerically the number of particles sharing the same cell as a function of time. In this paper, we provide a detailed discussion of the leading correlation corrections to the kinetic contribution of both the shear viscosity and the self-diffusion coefficient and determine analytically the probability that two and three particles are in the same collision cells for consecutive time steps. While our results for the self-diffusion coefficient are in general agreement with those of Ref. [26], there seem to be several misprints in [26], making a detailed comparison difficult.

The remainder of the paper is organized as follows. After a brief summary of the SRD algorithm in Sec. II, the hydrodynamic equations of a simple liquid are reviewed and the correct form of the constitutive equations are discussed in Sec. III. The consequences of the fact that angular momentum is not conserved in the SRD algorithm are summarized, and the correct form of the viscous stress tensor is discussed. In particular, it is emphasized that in two dimensions, there is no difference between the viscous stress tensor of a simple isotropic fluid and an SRD fluid. The slight differences in three dimensions leave the form of the Navier-Stokes unchanged, with only a reinterpretation of the coefficient of sound attenuation. Sec. IV contains a fairly detailed derivation of the dynamic correlation functions in a simple liquid. The discussion follows rather closely that of Ref. [27], but is included because several aspects of the derivation are a bit subtle and are generally not addressed in the literature. Explicit expressions for the vorticity, density, and entropy density dynamic correlations functions are presented. In Sec. V, these results are used to determine the shear and bulk viscosities and the thermal diffusivity. The agreement with the theoretical predictions summarized in Table I is excellent. Sec. VI contains a detailed discussion of the consequence of the breakdown of the molecular chaos approximation at short mean free paths. While correlation effects do not change the collisional contributions to the transport coefficients [21], they do dramatically increase the amplitude of the kinetic contribution. In addition to deriving the form of the leading correlation contributions to the shear viscosity and the self-diffusion coefficient, the probabilities that two (p_2) and three (p_3) particles are in the same collision cells at consecutive time steps are derived analytically in the limit $\lambda/a \to 0$. More generally, simulation results are used to show that p_2 is solely a function of λ/a. In the case of the shear viscosity, it is shown that inclusion of the leading correlation corrections yields results in surprisingly good agreement with measurements of the viscous stress correlations. For the self-diffusion coefficient, however, the correlation corrections for larger time intervals are large,

and dramatically increase the measured value of the self-diffusion coefficient for mean free paths smaller than the cell size. It is important to note that the correlation corrections considered here—arising from particles which collide with the same particles in consecutive time steps—are similar to those which occur in dense fluids interacting through soft potentials, and should therefore be interpreted as a "potential" or "collisional" contribution to the velocity or stress correlation functions rather than a precursor of the power-law (long-time) tails observable at longer times. We believe that it is important to distinguish between these two effects, since long time tails are also visible at large mean free paths where these corrections are negligibly small. Although the same approach can be used to calculate these contributions, the corresponding probabilities are much harder to estimate.

The results of this paper verify that we have an excellent understanding of the SRD algorithm at the kinetic level and that—with the exception of the self-diffusion coefficient—the analytic expressions for the transport coefficients given in Table I do indeed provide a very accurate description of the SRD fluid. Furthermore, the analysis of the dynamical structure factor and the dynamic entropy density correlation function verify directly that the algorithm satisfies the fluctuation-dissipation theorem. While this is to be expected for the current algorithm, which satisfies the necessary semi-detailed balance conditions [1, 17], verification studies of this type will be important for generalizations of the algorithm which model excluded volume effects through the use of biased multi-particle collision rules which depend on the local velocities and densities [28, 29].

II. MODEL

In the SRD algorithm, the fluid is modeled by particles with continuous spatial coordinates $\mathbf{r}_i(t)$ and velocities $\mathbf{v}_i(t)$. The system is coarse-grained into the cells of a regular lattice with no restriction on the number of particles in a cell. The evolution of the system consists of two steps: streaming and collision. In the streaming step, the coordinate of each particle is incremented by its displacement during the time step, Δt. Collisions are modeled by a simultaneous stochastic rotation of the relative velocities of every particle in each cell. As discussed in Refs. [4] and [17], a random shift of the particle coordinates (or, equivalently, the cell grid) before the collision step is required to ensure Galilean invariance. All particles are shifted by the same random vector with components in the interval $[-a/2, a/2]$ before the collision step. Particles are then shifted back to their original positions after the collision. If we denote the cell coordinate of the shifted particle i by ξ_i, the algorithm is summarized in the equations

$$\mathbf{r}_i(t+\Delta t) = \mathbf{r}_i(t) + \Delta t\, \mathbf{v}_i(t) \tag{1}$$

$$\mathbf{v}_i(t+\Delta t) = \mathbf{u}[\xi_i(t+\Delta t)] + \omega[\xi_i(t+\Delta t)]\,\{\mathbf{v}_i(t) - \mathbf{u}[\xi_i(t+\Delta t)]\}, \tag{2}$$

where $\omega(\xi_i)$ denotes a stochastic rotation matrix, and $\mathbf{u}(\xi_i) \equiv \frac{1}{M}\sum_{k\in\xi} \mathbf{v}_k$ is the mean velocity of the particles in cell ξ. All particles in the cell are subject to the same rotation, but the rotations in different cells are statistically independent. There is a great deal of freedom in how the rotation step is implemented, and any stochastic rotation matrix consistent with detailed balance can be used. In two dimensions, the stochastic rotation matrix, ω, is typically taken to be a rotation by an angle $\pm\alpha$, with probability 1/2 (see Refs. [4, 17, 19]). In three dimensions, one can perform rotations by an angle α about a randomly chosen direction, where all orientations of the random axis occur with equal probability (Model A in Ref. [20]).

III. HYDRODYNAMICS AND TRANSPORT COEFFICIENTS

There is a hydrodynamic mode associated with each conserved density in a fluid. For a simple liquid, the conserved quantities are the particle mass density, $\hat{\rho}(\mathbf{r};t)$, the momentum density, $\hat{\mathbf{g}}(\mathbf{r};t)$, and the energy density, $\hat{\varepsilon}(\mathbf{r};t)$, and the corresponding microscopic conservation laws are

$$\partial_t \hat{\rho}(\mathbf{r};t) + \partial_\alpha \hat{g}_\alpha(\mathbf{r};t) = 0, \tag{3}$$

$$\partial_t \hat{g}_\alpha(\mathbf{r};t) + \partial_\beta \hat{\sigma}_{\alpha\beta}(\mathbf{r};t) = 0, \tag{4}$$

and

$$\partial_t \hat{\varepsilon}(\mathbf{r};t) + \partial_\alpha \hat{J}_\alpha(\mathbf{r};t) = 0, \tag{5}$$

where $\hat{\sigma}_{\alpha\beta}(\mathbf{r};t)$ are the Cartesian components of the microscopic stress tensor and $\hat{J}_\alpha(\mathbf{r};t)$ is the α-component of the microscopic energy current density. While Eqs. (3)–(5) are microscopically exact, macroscopic constitutive relations

are required to close the system of equations. The constitutive equations relate local non-equilibrium averages of $\hat{g}(\mathbf{r};t)$, $\hat{\ }(\mathbf{r};t)$, and $\hat{\ }(\mathbf{r};t)$ to the local hydrodynamic variables, $(\mathbf{r};t) \equiv \langle \hat{\ }(\mathbf{r};t)\rangle$, $\mathbf{g}(\mathbf{r};t) \equiv \langle \hat{\mathbf{g}}(\mathbf{r};t)\rangle$, $(\mathbf{r};t) \equiv \langle \hat{\ }(\mathbf{r};t)\rangle$, and their gradients. For a simple isotropic liquid, the constitutive relations have the form [27, 30]

$$\langle \hat{g}(\mathbf{r};t)\rangle = \mathbf{g}(\mathbf{r};t); \tag{6}$$

$$\langle \hat{\ }(\mathbf{r};t)\rangle = p(\mathbf{r};t) \quad (\mathbf{r};t) \tag{7}$$

$$= p(\mathbf{r};t) \quad [\partial \mathbf{g}(\mathbf{r};t) + \partial \mathbf{g}(\mathbf{r};t) \quad (2/d) \quad \partial \mathbf{g}] \quad \partial \mathbf{g}; \tag{8}$$

$$\langle \hat{\ }(\mathbf{r};t)\rangle = [(+ p)/]\mathbf{g}(\mathbf{r};t) \quad \partial T(\mathbf{r};t); \tag{9}$$

where $p(\mathbf{r};t)$ and $T(\mathbf{r};t)$ are the local pressure and temperature fields, respectively. p is the equilibrium pressure and $$ is the equilibrium energy density; $$ and $$ are the kinematic shear and bulk viscosities, respectively, and $$ is the thermal conductivity. d is the spatial dimension, and $$ is the macroscopic viscous stress tensor. There are both non-derivative, reactive, and dissipative contributions to the constitutive relations. The form of the reactive terms can be inferred from Galilean invariance. The dissipative terms follow from an expansion of the current densities to first order in the gradients of the local conjugate forces $\mathbf{g}(\mathbf{r};t)$, $p(\mathbf{r};t)$, and $T(\mathbf{r};t)$; symmetry dictates the general form of these terms. Non-linear terms in the constitutive equations have been omitted because we only require the linear hydrodynamic equations in the following.

The local equilibrium averages of Eqs. (3)–(5), together with the constitutive relations given by Eqs. (6)–(9) provide a complete description of the hydrodynamics of the liquid. The resulting linearized Navier-Stokes equation is

$$\partial_t \mathbf{g}(\mathbf{r};t) + \partial p(\mathbf{r};t) \quad \partial^2 \mathbf{g}(\mathbf{r};t) \quad + \frac{d \quad 2}{d} \quad \partial \partial \mathbf{g}(\mathbf{r};t) = 0 : \tag{10}$$

The corresponding equations for the mass density and energy density are

$$\partial_t (\mathbf{r};t) + \partial \mathbf{g}(\mathbf{r};t) = 0; \tag{11}$$

and

$$\partial_t (\mathbf{r};t) + [(+ p)/]\partial \mathbf{g}(\mathbf{r};t) \quad \partial^2 T(\mathbf{r};t) = 0; \tag{12}$$

respectively.

Because of the cell structure introduced in SRD to define the collision environment, angular momentum is not conserved in a SRD collision. As a consequence, the macroscopic viscous stress tensor is not a symmetric function of the derivatives $\partial \mathbf{g}$, and instead of Eq. (8), the constitutive equation has the general form [22]

$$(\mathbf{r};t) = p(\mathbf{r};t) \quad {}_1 [\partial \mathbf{g}(\mathbf{r};t) + \partial \mathbf{g}(\mathbf{r};t) \quad (2/d) \quad \partial \mathbf{g}] \tag{13}$$

$$ {}_2 (\partial \mathbf{g}(\mathbf{r};t) \quad \partial \mathbf{g}(\mathbf{r};t)) \quad \partial \mathbf{g}; \tag{14}$$

where $_2$ is a new viscous transport coefficient associated with the non-symmetric part of the stress tensor. Because the kinetic contribution to the microscopic stress tensor is symmetric, $^{kin}_2 \quad 0$ and $^{kin}_1 \quad ^{kin}$. It is also easy to show that $^{kin} = 0$, so that the kinetic contribution to the macroscopic viscous stress tensor is

$$^{kin}(\mathbf{r};t) = \ ^{kin}[\partial \mathbf{g}(\mathbf{r};t) + \partial \mathbf{g}(\mathbf{r};t) \quad (2/d) \quad \partial \mathbf{g}(\mathbf{r};t)]: \tag{15}$$

In Ref. [22], it was also shown that the collisional contributions to the viscous transport coefficients fulfill the relation

$$[(d \quad 2)/d] \ ^{col}_1 \quad ^{col}_2 + \ ^{col} = 0; \tag{16}$$

and that the collision contribution to the macroscopic viscous stress tensor is

$$^{col}(\mathbf{r};t) = (\ ^{col}_1 + \ ^{col}_2)\partial \mathbf{g}(\mathbf{r};t) = \ ^{col}\partial \mathbf{g}(\mathbf{r};t) ; \tag{17}$$

up to a tensor with vanishing divergence, which will therefore not appear in the linearized hydrodynamic equations. The resulting linearized hydrodynamic equation for the momentum density is, therefore

$$\partial_t \mathbf{g}(\mathbf{r};t) + \partial p(\mathbf{r};t) \quad \partial^2 \mathbf{g}(\mathbf{r};t) \quad \frac{d \quad 2}{d} \ ^{kin} \partial \partial \mathbf{g}(\mathbf{r};t) = 0; \tag{18}$$

where $= \ ^{kin} + \ ^{col}$ and ^{kin} and ^{col} are the kinetic and collision contributions to the shear viscosity. The equations for the mass and energy densities remain unchanged. Comparison of Eq. (18) with Eq. (10) shows that the only difference between the Navier-Stokes equation for an isotropic liquid and an SRD fluid is in the coefficient of the $\partial \partial \mathbf{g}(\mathbf{r};t)$ term, where $$ is replaced by ^{kin}. The bulk viscosity does not appear in Eq. (18) because it is zero for the SRD algorithm. Note that both equations are identical in $d = 2$ and that the only difference in $d = 3$ is a correction to the sound attenuation coefficient associated with the viscous dissipation of longitudinal sound waves.

IV. DYNAMIC CORRELATIONS

Spontaneous thermal fluctuations of the density, $(\mathbf{r};t)$, momentum density, $\mathbf{g}(\mathbf{r};t)$, the energy density, $(\mathbf{r};t)$ are dynamically coupled, and an analysis of their dynamic correlation functions in the limit of small wave vectors and frequencies can be used to determine a fluid's transport coefficients. In particular, because it is easily measured in dynamic light scattering, x-ray, and neutron scattering experiments, the density-density correlation function | the dynamic structure factor | is one of the most widely used vehicles for probing the dynamic and transport properties of liquids [31].

In the following, we summarize the predictions of linearized hydrodynamics for the dynamic correlation functions of simple liquids in the hydrodynamic regime, and then use the results to analyze SRD simulation data in order to validate the theoretical results for the transport coefficients given in Table I. In particular, we provide in this way the first direct confirmation that the bulk viscosity is indeed zero for this model. Our discussion follows closely that of Ref. [27], but is included because the derivation using Laplace transforms is not widely used in the literature, and the detailed results are needed in the subsequent analysis. The starting point is the linearized hydrodynamic equations given in Eqs. (10), (11), and (12). There are four modes, one transverse shear mode, and three coupled longitudinal modes. In order to keep the analysis general, we include the bulk viscosity in this section.

Transverse fluctuations: Divide the momentum density $\mathbf{g}(\mathbf{r};t)$ into transverse and longitudinal components,

$$\mathbf{g}(\mathbf{r};t) = \mathbf{g}_k(\mathbf{r};t) + \mathbf{g}_?(\mathbf{r};t); \tag{19}$$

where $\mathbf{r} \quad \mathbf{g}_k(\mathbf{r};t) = 0$ and $\mathbf{r} \quad \mathbf{g}_?(\mathbf{r};t) = 0$. Taking the curl of the Navier-Stokes equation, the transverse component of the momentum density, $\mathbf{g}_?(\mathbf{r};t)$, is found to satisfy the diffusion equation

$$@_t \mathbf{g}_?(\mathbf{r};t) = \quad @^2 \mathbf{g}_?(\mathbf{r};t): \tag{20}$$

By performing the Fourier-Laplace transform ($\mathrm{Im}\, z > 0$)

$$\mathbf{g}_?(\mathbf{k};z) = \int_0^1 dt e^{izt} \int_V d\mathbf{r}\, e^{\,i\mathbf{k}\,\mathbf{r}} \mathbf{g}_?(\mathbf{r};t)\,; \tag{21}$$

the solution of the initial value problem, which describes the response of the transverse mode to an initial perturbation $\mathbf{g}_?(\mathbf{k};t=0)$ from equilibrium, is

$$_{g_?} \quad \mathbf{g}_?(\mathbf{k};z) = i \quad \mathbf{g}_?(\mathbf{k};t=0); \tag{22}$$

where $_{g_?} \quad z + ik^2$.

Longitudinal fluctuations: For the longitudinal components, it is convenient to introduce the variable $q(\mathbf{r};t)$, which is (T times) the entropy density,

$$q(\mathbf{r};t) \quad (\mathbf{r};t) \quad \frac{+ p}{} \quad (\mathbf{r};t) \tag{23}$$

in place of the energy density and use the relations

$$\mathbf{r}\, p(\mathbf{r};t) = \left(\frac{@p}{@}\right)_S \mathbf{r} \quad (\mathbf{r};t) + \frac{V}{T} \left(\frac{@p}{@S}\right) \mathbf{r}\, q(\mathbf{r};t) \tag{24}$$

and

$$\mathbf{r}\, T(\mathbf{r};t) = \left(\frac{@T}{@}\right)_S \mathbf{r} \quad (\mathbf{r};t) + \frac{V}{T} \left(\frac{@T}{@S}\right) \mathbf{r}\, q(\mathbf{r};t); \tag{25}$$

where S is the total entropy, to eliminate the pressure and temperature fields. Taking the Fourier-Laplace transform, the resulting coupled set of equations for the longitudinal modes can be written as

$$\begin{pmatrix} z & k & 0 \\ kc^2 & z + ik^2 D_\ & \frac{V}{T}\left(\frac{@p}{@S}\right) k \\ ik^2 \left(\frac{@T}{@}\right)_S & 0 & z + ik^2 \frac{}{c_v} \end{pmatrix} \begin{pmatrix} (\mathbf{k};z) \\ \mathbf{g}_k(\mathbf{k};z) \\ q(\mathbf{k};z) \end{pmatrix} = i \begin{pmatrix} (\mathbf{k};t=0) \\ \mathbf{g}_k(\mathbf{k};t=0) \\ q(\mathbf{k};t=0) \end{pmatrix}; \tag{26}$$

where, for example, $(k;t=0)$ $(k;t=0)$; is the equilibrium density, and $k = jkj$. Note that since $g_k(k;z)$ k k, the equation for the longitudinal component of the momentum density is a scalar equation. When writing Eq. (26), we have used the relations

$$c_v = \frac{T}{V}\frac{@S}{@T} \quad ; \qquad c_p = \frac{T}{V}\frac{@S}{@T}_p \quad ; \quad \text{and} \quad c^2 = \frac{@p}{@}_S = \frac{c_p}{c_v}\frac{@p}{@}_T \tag{27}$$

to simplify the nal expression. c is the adiabatic speed of sound, and D ; $= 2[(d\ 1)=d] +$. Eq. (26) describes how the longitudinal modes relax in response to initial perturbations $(k;t=0)$, $g(k;t=0)$, and $q(k;t=0)$. The zeros of the determinant of the coe cient matrix, , give the complex frequencies of the hydrodynamic modes of the system. For small wave vector k, the solutions of the resulting cubic equation are (up to terms of order k^3)

$$z = \ ck \ \frac{i}{2}k^2 \qquad \text{(sound poles)} \tag{28}$$

and

$$z = \ ik^2 D_T \qquad \text{(heat pole)}; \tag{29}$$

where $D_T = =(\ c_p)$ is the thermal di usivity; $= D_T(c_p=c_v\ 1) + D$;, is the sound attenuation coe cient. In deriving Eqs. (28) and (29), the thermodynamic relation

$$D_T c^2 (c_p=c_v\ 1) = \frac{V}{T}\frac{@T}{@}_S \frac{@p}{@S} \tag{30}$$

has been used.

Correlation functions: The matrix of dynamic correlation functions

$$S_{ij}(k;z) = \int_0^1 d(t\ t^0) \int_V d(r\ r^0) e^{iz(t\ t^0)\ ik\ (r\ r^0)} h[A_i(r;t)\ hA_ii][A_j(r^0;t^0)\ hA_jii] \tag{31}$$

is given by [27]

$$S_{ij}(k;z) = ik_B T(\ ^1)_{il}\ _{lj}(k); \tag{32}$$

where there is a sum over repeated indices. For the transverse modes, is simply a scalar function de ned in Eq. (22); for the longitudinal modes, however, it is a matrix, and the subscript indices denote the modes $(k;t=0)$, $g_k(k;t=0)$, and $q(k;t=0)$. $_{lj}(k)$ is the static susceptibility matrix.

The correlation function for the transverse mode follows from Eqs. (22) and (32) and $_{g_? g_?}(k) =$, and is given by

$$S_{g_? g_?}(k;z) = \frac{ik_B T}{z + ik^2} : \tag{33}$$

Taking the inverse Laplace transform,

$$S_{g_? g_?}(k;t) = \ k_B T e^{\ k^2 t} : \tag{34}$$

For the longitudinal modes, inverting and using the results $_{g_k}(k) = 0$, $_{g_k g_k}(k) =$, $\lim_{k!0}$ $(k) = (@\ =@p)_T$, $\lim_{k!0}{}_{qq}(k) = \ Tc_p$, and $\lim_{k!0}{}_q(k) = (T=m)(@\ =@T)_p$ (where m is the particle mass), one nds

$$S\ \ (k;z) = ik_B T\ \ \frac{@}{@p}_T \frac{c_v}{c_p}\frac{z + ik^2(\ + D_T[c_p=c_v\ 1])}{z^2\ \ c^2k^2 + izk^2} + 1\ \ \frac{c_v}{c_p}\ \ \frac{1}{z + ik^2 D_T} \tag{35}$$

and

$$S_{qq}(k;z) = ik_B T\frac{c_p T}{z + ik^2 D_T} \tag{36}$$

for the two scalar modes. Note that all non-vanishing static susceptibilities are symmetric in k, so that k-dependent corrections to $_{ij}$ are $O(k^2)$ and therefore negligible in these expressions. For details, the reader is referred to Refs. [27, 30].

The complete spectral transform of the time dependent density correlation function, the dynamic structure factor, $S(k;!)$, is obtained by setting $z = ! + i$ and taking the limit $! 0$ in Eq. (35). The final result is [27],

$$S(k;!) = 2k_B T \left(\frac{@}{@p}\right)_T \left[\frac{(c_v=c_p)c^2k^4}{(!^2 c^2k^2)^2 + (!k^2)^2} + \frac{(1 c_v=c_p)k^2D_T}{!^2 + (k^2D_T)^2} 1 \frac{c_v}{c_p} \frac{!^2 c^2k^2 k^2D_T}{(!^2 c^2k^2)^2 + (!k^2)^2}\right] : \quad (37)$$

In experiments, it is geneneralily not possible to measure $S(k;t)$ directly. In simulations, however, both $S(k;t)$ and $S(k;!)$ can be measured for a range of mean free paths and collision angles. The simplest way to determine $S(k;t)$ is to take the inverse Laplace transform of Eq. (35). In light of Eqs. (28) and (29), it is sufficient to keep terms $O(k)$ in real parts and $O(k^2)$ in the imaginary parts when evaluating the resulting contour integral. The final result is

$$S(k;t) = 2k_B T \left(\frac{@}{@p}\right)_T \frac{c_v}{c_p} e^{k^2t=2} \cos(ckt) + \frac{1}{2} + \frac{c_p}{c_v} 1 D_T \frac{k}{c} \sin(ckt) + 1 \frac{c_v}{c_p} e^{D_T k^2 t} : \quad (38)$$

Using Eq. (36), it can be shown that the correlation function for the entropy density, $q(r;t)$, is given by

$$S_{qq}(k;t) = c_p k_B T^2 e^{D_T k^2 t}: \quad (39)$$

Note that Eq. (39) provides an independent way to directly measure D_T.

These results remain valid for the SRD fluid. The only modification is that $D = 2[(d 1)=d]_{kin} + _{col}$, so that the sound attenuation coefficient is

$$= D_T \frac{c_p}{c_v} 1 + 2 \frac{d 1}{d} _{kin} + _{col}: \quad (40)$$

Note that in two-dimensions, the sound attenuation coefficient for a SRD fluid has the same functional dependence on D_T and $_{kin} + _{col}$ as an isotropic fluid with an ideal gas equation of state (for which $= 0$). Finally, since SRD describes an ideal fluid, $p = k_B T=m$ and $c_p = k_B=m + c_v = (d+2)k_B=2m$.

V. MEASUREMENTS

In our SRD simulations in two dimensions, the mass, momentum, and energy densities are measured at the cell level. The cell densities, $A^c(;t)$, are defined at the discrete set of coordinates $= am$, with $m = 1;:::;L$, for each spatial dimension [17]. A superscript c will be used to denote that the corresponding quantity is defined at the cell level. The Fourier transform of the cell variables are

$$A^c(k;t) = \sum_{} A^c(;t)e^{ik} ; \quad (41)$$

and the inverse transform is

$$A^c(;t) = \frac{1}{L^d} \sum_k A^c(k;t)e^{ ik} : \quad (42)$$

The Fourier-Laplace transforms of the corresponding dynamic correlation functions are

$$S^c_{ij}(k;z) = \int_0^1 d(t t^0) \sum e^{iz(t t^0) ik} h[A^c_i(;t) hA^c_ii][A^c_j(0;t^0) hA^c_ji]i : \quad (43)$$

Transverse fluctuations: Instead of the evaluating the correlation function of the transverse component of the momentum density, it is more convenient in simulations to measure the vorticity, $w(r;t) = r g_?(r;t)$. In two dimensions the vorticity is a scalar, $w_z(r;t)$, and the dynamic correlation function decays as

$$S^c_{w_z w_z}(k;t) = k^2 S^c_{g_? g_?}(k;t) = k_B T k^2 e^{k^2 t}: \quad (44)$$

Simulation results for the normalized vorticity correlation function for $=a \sqrt{k_B T=m} = 1:0$ with collision angle $= 120$ and $=a = 0:1$ with $= 60$ are shown in Figure 1. Here, as with all results presented in this paper, averages are taken over 400;000 iterations and five different random number seeds. The solid lines in Figure 1 are a

plot of Eq. (44) using the theoretical prediction for the shear viscosity (sum of kinetic and collisional contributions) given in Table I, for the smallest wave vector $k = (2\pi/L)(1;0)$. The agreement is excellent. We have also fitted the decay profiles for the lowest two wave vectors, namely to $k = (2\pi/L)(1;0)$ and $k = (2\pi/L)(0;1)$ with Eq. (44), and averaged the result to obtain estimates of the shear viscosity as a function of collision angle for different mean free paths. The results are presented in Figure 2, and, as expected, the agreement between measured viscosities and the expressions given in Table I is very good. These measurements clearly show that the theoretical expressions for the shear viscosity are accurate even for intermediate mean free paths.

Longitudinal fluctuations: Density fluctuations were measured at the cell level, and their Fourier-Laplace transform is taken to determine the structure factor. A naive implementation of this procedure gives wrong results in the large frequency region of the spectrum [24], resulting in finite contributions at all frequencies. This problem is well known to experimentalists [32], the solution is to first do a Fourier transform to obtain density-density correlations as a function of time, symmetrize this result around $t = 0$, and then perform the Laplace transform from -1 to 1. Results for the structure factor for $\tau/a = 1.0$ with collision angle $\alpha = 120°$ and $\tau/a = 0.1$ with $\alpha = 60°$ are shown in Figures 3(a) and 3(b), respectively. The solid lines are the theoretical expression given by Eq. (37) using $c = \sqrt{\gamma k_B T/m}$ and values for the transport coefficients obtained using the expressions in Table I, assuming that the bulk viscosity $\zeta = 0$. The agreement is excellent. There are three Lorentzian peaks, a central "Rayleigh peak" caused by the heat diffusion and two symmetrically displaced "Brillouin peaks" caused by the sound waves. The dotted vertical lines in the figures show the theoretically predicted frequencies of the adiabatic sound waves in a fluid with an ideal gas equation of state.

We have also measured time-dependent density correlations for various wave vectors. Figures 4(a) and 4(b) contain a comparison of the measured time-dependent density correlation functions with the predictions of Eq. (38), for $\tau/a = 1.0$ with collision angle $\alpha = 120°$ and $\tau/a = 0.5$ with $\alpha = 90°$. The agreement is excellent for all wave vectors considered. The bulk viscosity and thermal diffusivity were also independently measured by fitting these time dependent density correlations to the form given by Eq. (38) while using the theoretically predicted shear viscosity in the sound attenuation coefficient, keeping D_T and Γ as free parameters. The results are shown in Figure 5 as a function of the wave vector squared, for the same set of parameters as in Figure 4. Once again, the theoretical expression for D_T is confirmed, and the bulk viscosity is indeed zero.

In order to obtain an independent measure of the thermal diffusivity, we have measured the temporal behavior of the entropy correlations, $S^c_{qq}(k;t)$. The results are shown in Figure 6 for $\tau/a = 1.0$ with collision angle $\alpha = 120°$ and $\tau/a = 0.5$ with $\alpha = 90°$. As expected, these correrlations decay exponentially for all wave vectors considered. The solid lines in Figure 6 are a plot of Eq. (39) for the smallest wave vector $k = (2\pi/L)(1;0)$, using the theoretical prediction for the total thermal diffusivity, D_T (see Table I), and the agreement is again very good. As was done for the vorticity measurements, we have also fitted the decay profiles for the lowest two wave vectors with Eq. (39), and averaged the results to obtain independent measurements of the thermal diffusivity. The results for these measurements are shown in Figure 7 as a function of the collision angle α for $\tau/a = 0.5$ and $\tau/a = 1.0$. The theoretical values obtained using the formulae for D_T in Table I (sum of kinetic and collisional contributions) are shown in solid lines. These results are the first direct equilibrium measurements of the thermal diffusivity.

Finally, it is important to emphasize that just as for the shear viscosity, collisional contributions provide the dominant contribution to the thermal diffusivity at small mean free path. Figure 8 shows the theoretically predictions for both the collisional and kinetic contributions to the shear viscosity and thermal diffusitivity (inset) as a function of the mean free path τ/a. Collisional contributions to both transport coefficients are particularly important for small mean free paths and small M.

VI. CORRELATION EFFECTS

Green-Kubo relations for the SRD transport coefficients have been derived in Ref. [17] and analyzed in Refs. [19, 20, 21, 22], where it was shown that there are both kinetic and collisional contributions to the shear viscosity and the thermal diffusivity. The collisional contributions to these transport coefficients have been discussed in detail in Ref. [22].

The kinetic contribution to the transport coefficients have been derived by several groups [1, 5, 19, 20, 21] assuming molecular chaos. The results of these calculations are summarized in Table I. Simulation results for the shear viscosity and thermal diffusivity have generally been found to be in good agreement with these predictions. However, it is known that there are correlation effects for τ/a smaller than one [21]. They arise from correlated collisions between particles that are in the same collision cell for more than one time step. In the following, we expand on the discussion of Ref. [21] and calculate the first correlation corrections to both the viscosity and the self-diffusion coefficient explicitly. Similar calculations can in principle be done for the correlation contributions to thermal diffusivity. The reason that

these corrections to and D_T are generally negligible is that they are only significant in the small $=a$ regime, where the collisional contribution to the transport coefficients dominates.

Figure 8 shows a comparison of both kinetic and collisional contributions to shear viscosity and thermal diffusivity (inset) for $M = 3$ and $= 60$. Correlation effects would be most pronounced when both contributions are comparable, i.e. at a mean free path of $=a \simeq 0.25$ for and $=a \simeq 0.1$ for D_T (see Figure 8). On the other hand, because there are no collisional contributions to the self-diffusion coefficient, correlation corrections dramatically increase the value of this transport coefficient in the small $=a$ regime. It is important to note that there are no correlation corrections to the collisional contributions so that the expressions for the collisional shear viscosity [5, 21, 22] and collisional thermal diffusivity [21, 22] are exact.

In the following, we restrict ourselves to two dimensions; the same analysis, however, can also be used in three dimensions. Expressions for the shear viscosity and the self-diffusion coefficient in this section obtained in the molecular chaos approximation will include contributions from fluctuations in the number of particles per cell. However, when calculating correlation corrections, we will assume that the number of particles per cell, M, is fixed. Including these fluctuations is straightforward but tedious, and since it would not provide any additional insight into the underlying phenomena, we have decided to ignore this effect in the following.

A. Shear viscosity

The Green-Kubo relation for the kinetic contribution to the shear viscosity [21] is

$$^{kin} = k_B T \sum_{n=0}^{\infty} {}^{0} G(n) \tag{45}$$

where the prime indicates that the $t = 0$ contribution to the sum occurs with the weight 1/2, and

$$G(n) = \sum_{i,j} \langle v_{ix}(0) v_{iy}(0) v_{jx}(n) v_{jy}(n) \rangle / N (k_B T)^2 : \tag{46}$$

In the molecular chaos approximation [21],

$$G(n) \quad G_c(n) = 1 \quad 2\sin^2( ) M \quad 1 + e^{M} \quad /M^{n} : \tag{47}$$

Inserting this expression into Eq. (45) and summing, one obtains the kinetic contribution to viscosity given in Table I. Figure 9 contains a comparison of simulation results for $G(n)$ with the molecular chaos approximation Eq. (47). As can be seen, the first and the most important correlation contribution to ^{kin} occurs for $n = 2$. The functional form of this leading correlation correction, $G(2) = G(2) \quad G_c(2)$, can be calculated analytically.

As illustrated schematically in Figure 10, there are six distinct particle configurations which contribute. The first two, shown in Figures 10(1) and 10(2) occur when $i = j$ in the sum in Eq. (46); we will call these the diagonal contribution. In Figure 10(1), particle k is in the same collision cell as i for both $t = 2$ and $t =$. In Figure10(2), two distinct particles, labeled k and l, are in the same collision cell as i at both $t = 2$ and $t =$. Other (off-diagonal) contributions, which occur for $i \neq j$, are given in Figure 10(3)–(6). These contributions are significant only at small mean free paths, since their amplitudes are proportional to the probability that two or more particles are in the same collision cell for multiple times.

1. Diagonal contributions

The first diagonal contribution, which we denote by $G_1(2)$, occurs when two particles, with indices i and k, are in the same collision cell at both $t =$ and $t = 2$. The probability for this to occur is p_2; p_2 is calculated in the $=a \to 0$ limit in Appendix A. In two dimensions the velocity of particle i at time $t = n$ is related to the velocities of its collision partners at $t = (n \quad 1)$ by

$$\begin{aligned} v_{ix}(n) &= c v_{ix}([n \quad 1]) + \frac{1 \quad c}{M} \sum_k v_{kx}([n \quad 1]) + s\, v_{iy}([n \quad 1]) \quad \frac{1}{M} \sum_k v_{ky}([n \quad 1]) \\ v_{iy}(n) &= c v_{iy}([n \quad 1]) + \frac{1 \quad c}{M} \sum_k v_{ky}([n \quad 1]) \quad s\, v_{ix}([n \quad 1]) \quad \frac{1}{M} \sum_k v_{kx}([n \quad 1]) ; \end{aligned} \tag{48}$$

where $c = \cos(\ )$ and $s = \sin(\ )$. Using Eq. (48) to relate the velocities at $t = 2\ $ to those at $t = \ $, we have

$$G_1(2\ ) = 2p_2(M\ \ 1)\sum_i v_{ix}(0)v_{iy}(0)\,[\ _1 v_{ix}(\ ) + \ _2 v_{iy}(\ )]\ \frac{1\ \ c}{M}v_{ky}(\ ) + \frac{s}{M}v_{kx}(\ )\ \ =N\ (k_B T)^2; \tag{49}$$

where $\ _1 = 1=M + c(1\ \ 1=M)$ and $\ _2 = s(1\ \ 1=M)$, and the factor $(M\ \ 1)$ accounts for the sum over $k \in i$ and the factor 2 comes from the fact that i and k can interchange roles. The equilibrium average in Eq. (49) entails the average over all initial coordinates and velocities (at $t = 0$) as well as averages over the stochastic rotations $(\ )$ at $t = \ $ and $t = 2\ $. Performing the average over the collision angle at $t = 2\ $ in Eq. (49) removes all terms linear in s, so that

$$G_1(2\ ) = \frac{2p_2(M\ \ 1)}{M}\sum_i \langle v_{ix}(0)v_{iy}(0)\,[\ _1(1\ \ c)v_{ix}(\ )v_{ky}(\ ) + \ _2 s v_{iy}(\ )v_{kx}(\ )]\rangle =N\ (k_B T)^2: \tag{50}$$

Using Eq. (48) once again with $n = 1$,

$$G_1(2\ ) = \frac{2p_2(M\ \ 1)}{M}\sum_i \Big\langle v_{ix}(0)v_{iy}(0)\ \ \ _1(1\ \ c)\,[\ _1 v_{ix}(0) + \ _2 v_{iy}(0)]\ \ \frac{1\ \ c}{M}v_{iy}(0) + \frac{s}{M}v_{ix}(0)$$
$$+\ \ \ _2 s\,[\ _1 v_{iy}(0)\ \ \ _2 v_{ix}(0)]\ \ \frac{1\ \ c}{M}v_{ix}(0)\ \ \ \frac{s}{M}v_{iy}(0)\ \ \Big\rangle =N\ (k_B T)^2: \tag{51}$$

Averaging now over the collision angle at $t = \ $ and the particle velocities and coordinates at $t = 0$ yields

$$G_1(2\ ) = \frac{2p_2(M\ \ 1)}{M^{\ 2}}\,[\ _1(1\ \ c) + \ _2 s]^2\ : \tag{52}$$

The other diagonal contribution, which we will denote as $G_2(2\ )$, arises when three particles, with indices i, k and l, are in the same collision cell at $t = \ $ and $t = 2\ $. The probability that three particles are in the same collision cell in consecutive time steps will be denoted by p_3; p_3 is calculated in the $\ = a\ !\ 0$ limit in Appendix B. Using Eq. (48),

$$G_2(2\ ) = p_3(M\ \ 1)(M\ \ 2)\sum_i v_{ix}(0)v_{iy}(0)\ \ \frac{1\ \ c}{M}v_{kx}(\ )\ \ \frac{s}{M}v_{ky}(\ )\ \ \frac{1\ \ c}{M}v_{ly}(\ ) + \frac{s}{M}v_{lx}(\ )\ \ =N\ (k_B T)^2; \tag{53}$$

where the prefactor $(M\ \ 1)(M\ \ 2)$ comes from the double sum over $k; l$. Averaging over the collision angle at $t = 2\ $ yields

$$G_2(2\ ) = \frac{p_3(M\ \ 1)(M\ \ 2)}{M^{\ 2}}\sum_i v_{ix}(0)v_{iy}(0)\ \ [1\ \ c]^2 v_{kx}(\ )v_{ly}(\ )\ \ s^2 v_{ky}(\ )v_{lx}(\ )\ \ =N\ (k_B T)^2: \tag{54}$$

Finally, using Eq. (48) again and averaging over the collision angle at $t = \ $ and velocities and coordinates at $t = 0$ yields

$$G_2(2\ ) = \frac{p_3(M\ \ 1)(M\ \ 2)}{M^{\ 4}}\,[2c(c\ \ 1)]^2\ : \tag{55}$$

2. Off-diagonal contributions

The analysis of these contributions is very similar to that which was used to evaluate the diagonal contributions, so we provide fewer details than in the previous subsection. There are four off-diagonal contributions, all of which contribute with probability p_2. The first, $G_3(2\ )$, shown in Figure 10 (3), can be written as

$$G_3(2\ ) = 2p_2(M\ \ 1)(M\ \ 2)\sum_i v_{ix}(0)v_{iy}(0)\ \ \frac{1\ \ c}{M}v_{ix}(\ )\ \ \frac{s}{M}v_{iy}(\ )\ \ \frac{1\ \ c}{M}v_{ky}(\ ) + \frac{s}{M}v_{kx}(\ )\ \ =N\ (k_B T)^2\ ; \tag{56}$$

where the factor $2(M\ \ 1)(M\ \ 2)$ accounts for i and k interchanging roles and the double sum over j and k. Following the same procedure as was used to evaluate $G_1(2\ )$ and $G_2(2\ )$, we have

$$G_3(2\ ) = \frac{2p_2(M\ \ 1)(M\ \ 2)}{M^{\ 3}}\,[2c(c\ \ 1)][\ _1(1\ \ c) + \ _2 s]\ : \tag{57}$$

The second contribution, $G_4(2\ )$, depicted Figure 10(4) can be written as

$$G_4(2\ ) = 2p_2(M\ \ 1)(M\ \ 2)\sum_i v_{ix}(0)v_{iy}(0)[\ _1v_{jx}(\ ) + \ _2v_{jy}(\ )]\ \frac{1\ \ c}{M}v_{ky}(\ ) + \frac{s}{M}v_{kx}(\ )\ \ =N\ (k_B\ T)^2; \quad (58)$$

where the prefactor is similar to that of $G_3(2\ )$. Using this result, it is straightforward to show that

$$G_4(2\ ) = \frac{2p_2(M\ \ 1)(M\ \ 2)}{M^{\ 3}}[2c(c\ \ 1)][\ _1(1\ \ c) + \ _2s]: \quad (59)$$

The third contribution involves the configuration shown in Figure 10(5). It is similar to the diagonal contribution $G_2(2\ )$ except for the fact that the particle with index i is not in the same shifted cell as k and l at time $t = 2\ $. Only two particles are in the same collision cell for consecutive time steps, so that the relevant probability is p_2. By analogy with the expression for $G_2(2\ )$,

$$G_5(2\ ) = \frac{p_2(M\ \ 1)(M\ \ 2)(M\ \ 3)}{M^{\ 4}}[2c(c\ \ 1)]^2\ ; \quad (60)$$

where the factor of $(M\ \ 3)$ comes from the additional sum over j with the constraints $i \neq j \neq k \neq l$.

The final contribution, $G_6(2\ )$, occurs when i and j are in the same collision cell at both $t = 2\ $ and $t = \ $ (see Figure 10(6)). This contribution is given by

$$G_6(2\ ) = 2p_2(M\ \ 1)\sum_i v_{ix}(0)v_{iy}(0)\ \ \frac{1\ \ c}{M}v_{ix}(\ )\ \ \frac{s}{M}v_{iy}(\ )\ \ [\ _1v_{jy}(\ )\ \ \ _2v_{jx}(\ )]\ =N\ (k_B\ T)^2; \quad (61)$$

where the factor $2(M\ \ 1)$ accounts for the sum over j and interchanging i and j. Following the same procedure as for the other contributions, we find

$$G_6(2\ ) = \frac{2p_2(M\ \ 1)}{M^{\ 2}}[\ _1(1\ \ c) + \ _2s]: \quad (62)$$

The total correlation enhancement is obtained by summing these six contributions,

$$G(2\ ) = \sum_{n=1}^{6} G_n(2\ ): \quad (63)$$

Note that the only dependence on the temperature and time step occur in the probabilities p_2 and p_3. The measured correlation contributions to the shear viscosity are shown in Figure 11 as a function of $=a$ for $= 60\ , 90\ ,$ and $120\ $. Using the $=a\ !\ 0$ values for the probabilities p_2 and p_3 calculated in Appendices A and B, one finds

$$G(2\ ) = \sum_{n=1}^{6} G_n(2\ ) = \frac{M\ \ 1}{9M^{\ 4}}\ f4M\ [1+\cos(\ )]g^2 + 7(2\ \ M\ )\cos^2(\ )\ : \quad (64)$$

and

$$_{kin}\ ,\ k_B\ T\ \ \left(\sum_{n=0}^{1}\ ^0G_c(n\ ) + \ G(2\ )\right) \quad (65)$$

for the shear viscosity. As can be seen from Figure 11, the results obtained using Eq. (64) (asterisks) are in excellent agreement with simulation data in the limit of zero mean free path. More generally, we have determined the probabilities p_2 and p_3 numerically and have found that they depend only on the value of the mean free path, , and not on and T individually (see inset of Figure 14 for a plot of p_2 as a function of $=a$). Finally, these results can be used in Eq. (63) to obtain an estimate of the correlation contribution $G(2\ )$ for arbitrary . The asterisks in Figure 9 show the results of this procedure, and as might be expected, the agreement is excellent. Finally, simulation results for the total kinetic contribution to the viscosity as a function of time are shown in the inset to Figure 9. The filled squares ( ) are the predictions of molecular chaos approximation, and asterisks are a plot of Eq. (65). The incipient long-time tail is clearly visible in the figure. This is one of the reasons that it has been difficult to obtain good estimates for the "bare" kinetic contribution to the transport coefficients. In principle, the methods used to determine $G(2\ )$ can also be employed to determine these correlation contributions at greater time lags. The corresponding probabilities, however, that particles become collision neighbors after a finite time interval are much harder to determine, since they depend in detail to relative probabilities of various fluctuating flow configurations.

B. Self-diffusion coefficient

The Green-Kubo relation for the self-diffusion coefficient is [19]

$$D = \frac{k_B T}{2} \sum_{n=0}^{\infty}{}' H(n\tau), \tag{66}$$

and

$$H(n\tau) = \langle v_i(0) \cdot v_i(n\tau) \rangle / (k_B T). \tag{67}$$

Since the self-diffusion coefficient is a single-particle property, there is no sum over i in Eq. (66). In the molecular chaos approximation,

$$H(n\tau) \to H_c(n\tau) = 2\cos(\chi) + (1 - \cos(\chi))\left(1 - e^{-M\chi/M}\right)^n, \tag{68}$$

Inserting Eq. (68) into Eq. (66) and summing the resulting geometric series, one can obtain the expression for the self-diffusion coefficient in two dimensions given in Table I.

The self-diffusion coefficient is unique in that there is no "collisional" contribution; as a result, correlation corrections are much more important at small mean free path and can lead to large corrections to the results obtained using the molecular chaos approximation. Corrections to this result occur when two or more particles occupy the same collision cell at different time steps. Figure 12 contains a comparison of the molecular chaos approximation for the velocity auto-correlation function, $H(n\tau)$, ( ) with simulation results ( ).

The first of these correlation corrections, $H(2\tau)$, occurs at $t = 2\tau$. The contributing configuration, in which two particles, i and k, are in the same (shifted) cell at both $t = \tau$ and $t = 2\tau$, is shown in Figure 13; the probability for this to occur is again p_2. The contribution of this configuration to the velocity auto-correlation function is

$$H(2\tau) = 2p_2(M-1)\left\langle v_{ix}(0)\left(\frac{1-c}{M}v_{kx}(\tau) - \frac{s}{M}v_{ky}(\tau)\right)\right\rangle/(k_B T), \tag{69}$$

where the factor 2 arises since both x and y components contribute; the factor $M-1$ accounts for the fact that $k \neq i$ can correspond to any of the $M-1$ particles. Following the procedure outlined in the discussion of correlation effects to the viscosity, it is straightforward to evaluate the averages in Eq. (69). The final result is

$$H(2\tau) = 2p_2(M-1)\left(\frac{1-c}{M}\right)^2 = \frac{8(M-1)}{9M^2}[1-\cos(\chi)]^2. \tag{70}$$

This is the only correlation correction at $t = 2\tau$. At longer times there are similar higher order correlation effects arising, for example, when two particles are in the same shifted cell for three time steps, etc. It is straightforward but tedious to calculate these contributions. The probability p_2 in Eq. (70) is determined analytically in the limit $\ell/a \to 0$ in Appendix A, where it is shown that $p_2 = (2/3)^d$ in d dimensions. For finite ℓ/a, it can be measured in simulations. It should be noted that p_2 is related to the quantity $_1$ of Ref. [26], which denotes the number of particles that are neighbors of a given particle for two consecutive time steps; more precisely, $p_2 = (_1 - 1)/(M-1)$.

Figure 14 is a plot of simulation results for $H(2\tau)$ as a function of ℓ/a for three different values of the collision angle χ. The asterisks ( ) are result of Eq. (70) using the $\ell/a \to 0$ prediction $p_2 = 4/9$; as can be seen, the agreement with simulation data is excellent. The inset in Figure 14 shows p_2 as a function of ℓ/a. The value for the probability p_2 in the limit $\ell/a \to 0$ is in excellent agreement with the result derived in Appendix A.

We have only considered correlation effects caused by two particles occupying the same collision cell for the two consecutive time steps. In fact, additional contributions arise any time two particles find themselves in the same collision cell for more than two time steps or after any number of time steps. It is interesting to see just how important these latter contributions are by summing up all possible contributions from $H(2\tau)$ and $H_c(\ )$. Figure 15 shows the contributions for the first five time steps in the series. In this approximation, the self-diffusion constant can be written as

$$D \simeq \frac{k_B T}{2} \sum_{n=0}^{\infty}{}' \left[H_c(n\tau) + \tilde{H}(n\tau) \right] \tag{71}$$

where

$$\tilde{H}(n\tau) = \begin{cases} 0; & n \leq 1 \\ H(2\tau); & n = 2 \\ H(2\tau)H_c(\tau); & n = 3 \\ (1/2)\,H(2\tau)^2 + (3/2)\,H(2\tau)H_c(2\tau); & n = 4 \\ (3/4)\,H(2\tau)^2 H_c(\tau) + 2\,H(2\tau)H_c(3\tau); & n = 5 \\ \vdots & \end{cases} \tag{72}$$

are the contributions shown in Figure 15. The solid lines in the figure represent the factor $H(2\tau)$, and the dashed lines represent the factor $H_c(\tau)$ from time steps where particles are not correlated and the molecular chaos approximation is valid. The resulting contribution of Eq. (72) is shown in Figure 12 by asterisks ($*$). The agreement with simulations at $t = 2\tau$ is perfect, as expected, and the prediction for larger time intervals is improved. It would be extremely interesting to extend the analysis to consider the contributions of correlation effects at larger time intervals that lead to long time tails in the velocity auto-correlation function [33].

VII. CONCLUSION

This paper contains the first detailed analysis of equilibrium dynamic correlation functions using the SRD algorithm. The dynamic structure factor, vorticity and entropy density correlation functions were measured and used to provide unbiased estimates for the viscosity, thermal diffusivity, and bulk viscosity. The results are in good agreement with earlier numerical and theoretical results, and provide the first direct verification that the bulk viscosity is zero for this algorithm.

Table I contains a complete summary of analytical results for the transport coefficients of this model, and the results of this paper verify that we have an excellent understanding of the SRD algorithm at the kinetic level and that the analytic expressions for the transport coefficients do indeed provide a very accurate description of the SRD fluid. Furthermore, the analysis of the dynamical structure factor and the dynamic entropy density correlation function verify directly that the algorithm satisfies the fluctuation-dissipation theorem. Verification studies of this type will be important for generalizations of the algorithm which model excluded volume effects through the use of biased multi-particle collision rules which depend on the local velocities and densities.

Finally, corrections to the self-diffusion coefficient and shear viscosity arising from the breakdown of the molecular chaos approximation at small mean free paths were analyzed. In addition to deriving the form of the leading correlation corrections to these transport coefficients, the probabilities that two and three particles remain collision partners for consecutive time steps are derived analytically in the limit of small mean free path. Extensions of this approach could be used to study the development of long time tails in the velocity and stress auto-correlation functions.

Acknowledgments

Support from the National Science Foundation under grant No. DMR-0513393 and ND EPSCoR through NSF grant EPS-0132289, is greatfully acknowledged.

APPENDIX A: CALCULATION OF p_2

Random grid shifts in x- and y-directions are statistically independent. We therefore first calculate the contribution from shifts in the x-direction; the final probability for general shifts in two-dimensions is then obtained by squaring this one-dimensional result. The following calculations are done in the limit $\epsilon/a \to 0$, so that the particles do not move between time steps.

There are three different ways for two particles to be in the same shifted cell at consecutive time steps (see Figure 16). If the shifted cell index at $t = \tau$, $\xi_s(\tau)$ is zero, then $\xi_s(2\tau)$ can be either $-a; 0$ or a. Because these are mutually exclusive events, the probability of each scenario has to be calculated separately and then summed.

1. $\xi_s(\tau) = 0, \xi_s(2\tau) = 0$

The situation is shown pictorially in Figure 16(a). The probability p_2^A that two particles are in cell $\xi_s = 0$ for two consecutive time steps can be written as

$$p_2^A = \frac{1}{a^4}\int_{-a/2}^{a/2} d\xi_2 \int_{-a/2}^{a/2} d\xi_1 \int_{-1}^{a+\xi_1} dx_1 \int_{-1}^{a+\xi_1} dx_2 \; (x_1 - \xi_2)\left[1 - (x_1 - a - \xi_2)\right] (x_2 - \xi_2)\left[1 - (x_2 - a - \xi_2)\right]; \tag{A1}$$

where $_1$ and $_2$ are the shifts at times and 2 , respectively. Making the substitutions X_1 x_1 $_1$ and X_2 x_2 $_1$, Eq. (A1) becomes

$$p_2^A = \frac{1}{a^4} \int_{a=2}^{a=2} d_2 \int_{a=2}^{a=2} d_1 \int_0^a dX_1 \int_0^a dX_2 \quad (X_1 + _1 \quad _2)[1 \quad (X_1 \quad a + _1 \quad _2)]$$
$$(X_2 + _1 \quad _2)[1 \quad (X_2 \quad a + _1 \quad _2)]: \qquad (A2)$$

To simplify further, introduce $_1$ $_1$ $_2$ and integrate X_1 and X_2 over the portion of the square where the integrand is non-zero. This yields

$$p_2^A = \frac{1}{a^4} \int_{a=2}^{a=2} d_2 \int_{a=2}^{a=2} d_1 (a \quad j_1 j)^2 : \qquad (A3)$$

Using, finally,

$$\int_{a=2}^{a=2} d_2 \int_{a=2}^{a=2} d_1 = a^2; \qquad (A4)$$

$$\int_{a=2}^{a=2} d_2 \int_{a=2}^{a=2} d_1 j_1 j = \frac{a^3}{3} \qquad (A5)$$

$$\int_{a=2}^{a=2} d_2 \int_{a=2}^{a=2} d_1 \ _1^2 = \frac{a^4}{6}; \qquad (A6)$$

Eq. (A3) gives

$$p_2^A = 1 \quad \frac{2}{3} + \frac{1}{6} = \frac{1}{2} : \qquad (A7)$$

2. $_s( ) = 0$, $_s(2) = a$

This situation is illustrated in Figure 16b. The probability p_2^B that two particles are in cell $_s = 0$ at $t =$ and $_s = a$ at $t = 2$ is

$$p_2^B = \frac{1}{a^4} \int_{a=2}^{a=2} d_2 \int_{a=2}^{a=2} d_1 \int_{_1}^{a+ _1} dx_1 \int_{_1}^{a+ _1} dx_2 \quad (x_1 + a \quad _2)[1 \quad (x_1 \quad _2)]$$
$$(x_2 + a \quad _2)[1 \quad (x_2 \quad _2)] : \qquad (A8)$$

Making the substitutions X_1 x_1 $_1$ and X_2 x_2 $_1$, Eq. (A8) becomes

$$p_2^B = \frac{1}{a^4} \int_{a=2}^{a=2} d_2 \int_{a=2}^{a=2} d_1 \int_0^a dX_1 \int_0^a dX_2 \quad (X_1 + a + _1 \quad _2)[1 \quad (X_1 + _1 \quad _2)]$$
$$(X_2 + a + _1 \quad _2)[1 \quad (X_2 + _1 \quad _2)] : \qquad (A9)$$

As in the previous subsection, introducing $_1$ $_1$ $_2$ and integrating X_1 and X_2 over the portion of the square where the integrand is non-zero yields

$$p_2^B = \frac{1}{a^4} \int_{a=2}^{a=2} d_2 \int_{a=2}^{a=2} d_1 j_1 j^2 \quad (\quad _1) = \frac{1}{12} : \qquad (A10)$$

3. $_s( ) = 0$, $_s(2) = a$

Referring to Figure 16c. the probability p_2^C that two particles are in cell $_s = 0$ at $t =$ and $_s = a$ at $t = 2$ is

$$p_2^C = \frac{1}{a^4} \int_{a=2}^{a=2} d_2 \int_{a=2}^{a=2} d_1 \int_{_1}^{a+ _1} dx_1 \int_{_1}^{a+ _1} dx_2 \quad (x_1 \quad a + _2)[1 \quad (x_1 \quad 2a + _2)]$$
$$(x_2 \quad a + _2)[1 \quad (x_2 \quad 2a + _2)] : \qquad (A11)$$

Making the same change of variables as in the previous two cases, Eq. (A11) becomes

$$p_2^C = \frac{1}{a^4} \int_{a=2}^{a=2} d_2 \int_{a=2}^{a=2} d_1 \int_0^a dX_1 \int_0^a dX_2 \quad (X_1 \;\; a + \;_1 + \;_2)[1 \quad (X_1 \;\; 2a + \;_1 + \;_2)]$$
$$(X_2 \;\; a + \;_1 + \;_2)[1 \quad (X_2 \;\; 2a + \;_1 + \;_2)] : \qquad \text{(A12)}$$

Introducing now $\;_2 \quad \;_1 + \;_2$ and performing the integrals over X_1 and X_2 yields

$$p_2^C = \frac{1}{a^4} \int_{a=2}^{a=2} d_2 \int_{a=2}^{a=2} d_1 \;_2^2 \;\; (\;_2) = \frac{1}{12} : \qquad \text{(A13)}$$

The final result in two dimensions is obtained by summing the results given in Eqs. (A7), (A10) and (A13), and squaring, so that

$$p_2 = (p_2^A + p_2^B + p_2^C)^2 = \frac{4}{9} : \qquad \text{(A14)}$$

APPENDIX B: CALCULATION OF p_3

The calculation of p_3 in the limit $=a \;! \; 0$ is similar to that of p_2 in the previous Appendix. There are three scenarios, as depicted in Figure 16 (with three particles instead of two). p_3^A is the probability that three particles are in the $_s = 0$ for two consecutive time steps:

$$p_3^A = \frac{1}{a^5} \int_{a=2}^{a=2} d_2 \int_{a=2}^{a=2} d_1 \int_{\;_1}^{a+\;_1} dx_1 \int_{\;_1}^{a+\;_1} dx_2 \int_{\;_1}^{a+\;_1} dx_3 \quad (x_1 \quad \;_2)[1 \quad (x_1 \;\; a \quad \;_2)]$$
$$(x_2 \quad \;_2)[1 \quad (x_2 \;\; a \quad \;_2)]$$
$$(x_3 \quad \;_2)[1 \quad (x_3 \;\; a \quad \;_2)] : \qquad \text{(B1)}$$

To evaluate this integral, make the same change of variables to X_1 and X_2 as in the previous Appendix and introduce $\;_1 = \;_1 \quad \;_2$. Performing the X integrals then gives

$$p_3^A = \frac{1}{a^5} \int_{a=2}^{a=2} d_2 \int_{a=2}^{a=2} d_1 (a \quad j\;_1 j)^3 : \qquad \text{(B2)}$$

Using

$$\int_{a=2}^{a=2} d_2 \int_{a=2}^{a=2} d_1 j\;_1 j^3 = \frac{a^5}{10} \qquad \text{(B3)}$$

and Eqs. (A4), (A5), (A6) and (B3), Eq. (B2) yields

$$p_3^A = 1 \quad 1 + \frac{1}{2} \quad \frac{1}{10} = \frac{2}{5} : \qquad \text{(B4)}$$

The calculations of p_3^B and p_3^C are similar to those outlined in Sections A 2 and A 3, and both are equal to $1=20$. Summing these results,

$$p_3 = \; p_3^A + p_3^B + p_3^C \;^2 = \frac{1}{4} \qquad \text{(B5)}$$

in two dimensions.

---

[1] A. Malevanets and R. Kapral, J. Chem. Phys. 110, 8605 (1999).
[2] A. Malevanets and R. Kapral, J. Chem. Phys. 112, 7260 (2000).
[3] G. A. Bird, Molecular Gas Dynamics and the Direct Simulation of Gas Flows (Oxford University Press, USA, 1994).
[4] T. Ihle and D. M. Kroll, Phys. Rev. E 63, 020201 (2001).

[5] C. M. Pooley and J. M. Yeomans, J. Phys. Chem. B 109, 6505 (2005).
[6] J. F. Ryder, Ph.D. thesis, University of Oxford (2005).
[7] N. Kikuchi, A. Gent, and J. M. Yeomans, Eur. Phys. J. E 9, 63 (2002).
[8] R. G. Winkler, K. Mussawisade, M. Ripoll, and G. Gompper, J. Phys.: Condens. Matter 16, 3941 (2004).
[9] M. A. Webster and J. M. Yeomans, J. Chem. Phys. 122, 164903 (2005).
[10] E. Falck, J. M. Lahtinen, I. Vattulainen, and T. Ala-Nissila, Eur. Phys. J. E 13, 267 (2004).
[11] Y. Inoue, Y. Chen, and H. Ohashi, J. Stat. Phys. 107, 85 (2002).
[12] J. T. Padding and A. A. Louis, Phys. Rev. Lett. 93, 220601 (2004).
[13] M. Hecht, J. Harting, T. Ihle, and H. J. Herrmann, Phys. Rev. E 72, 011408 (2005).
[14] J. T. Padding and A. A. Louis, cond-mat/0603391.
[15] H. Noguchi and G. Gompper, Phys. Rev. Lett. 93, 258102 (2004).
[16] H. Noguchi and G. Gompper, Phys. Rev. E 72, 011901 (2005).
[17] T. Ihle and D. M. Kroll, Phys. Rev. E 67, 066705 (2003).
[18] N. Kikuchi, C. M. Pooley, J. F. Ryder, and J. M. Yeomans, J. Chem. Phys. 119, 6388 (2003).
[19] T. Ihle and D. M. Kroll, Phys. Rev. E 67, 066706 (2003).
[20] E. Tuzel, M. Strauss, T. Ihle, and D. M. Kroll, Phys. Rev. E 68, 036701 (2003).
[21] T. Ihle, E. Tuzel, and D. M. Kroll, Phys. Rev. E 70, 035701 (2004).
[22] T. Ihle, E. Tuzel, and D. M. Kroll, Phys. Rev. E 72, 046707 (2005).
[23] E. Allahyarov and G. Gompper, Phys. Rev. E 66, 036702 (2002).
[24] Y. Inoue, Y. Chen, and H. Ohashi, Comp. Phys. Commun. 153, 66 (2003).
[25] M. Ripoll, K. Mussawisade, R. G. Winkler, and G. Gompper, Europhys. Lett. 68, 106 (2004).
[26] M. Ripoll, K. Mussawisade, R. G. Winkler, and G. Gompper, Phys. Rev. E 72, 016701 (2005).
[27] D. Forster, Hydrodynamic Fluctuations, Broken Symmetry, and Correlation Functions (W. A. Benjamin, Reading, 1975).
[28] T. Ihle, E. Tuzel, and D. M. Kroll, Europhys. Lett. 73, 664 (2006).
[29] E. Tuzel, T. Ihle, and D. M. Kroll, cond-mat/0511312, to be published in Math. Comp. Simul.
[30] J. P. Boon and S. Yip, Molecular Hydrodynamics (Dover Publications, New York, 1992).
[31] B. J. Berne and R. Pecora, Dynamic light scattering: with applications to chemistry, biology and physics (John Wiley & Sons, New York, 1976).
[32] M. Tekmen, private communication.
[33] J. R. Dorfman and E. G. D. Cohen, Phys. Rev. Lett. 25, 1257 (1970).
[34] C. M. Pooley, Ph.D. thesis, University of Oxford (2003).

TABLE I: Theoretical expressions for the shear viscosity , the thermal diffusivity D_T, and the self-diffusion coefficient D, in both two and three dimensions. M denotes the average number of particles per cell, is the collision angle, k_B is Boltzman's constant, T is the temperature and is the time step. Except for self-diffusion constant, where there is no collisional contribution, both the kinetic and collisional contributions are listed. The expressions for shear viscosity and self-diffusion coefficient include fluctuation corrections for small M; however, for brevity the relations for thermal diffusivity are correct only up to $O(1/M)$ and $O(1/M^2)$ for the kinetic and collisional contributions, respectively. Both kinetic and collisional contributions to shear viscosity have been calculated using two complementary approaches, equilibrium Green-Kubo relations [17, 19, 20, 21, 22] and a non-equilibrium approach [5, 18]. Results from both approaches are in complete agreement. Similarly, the kinetic contribution to thermal diffusivity has also been calculated using these two approaches. The predictions of both approaches are identical in two dimensions and agree up to (and including) $O(1/M)$ in three dimensions; higher order contributions in $1/M$ were not considered in the Green-Kubo approach. The kinetic contribution to thermal diffusivity calculated using the non-equilibrium approach was taken from Ref. [34], since there appear to be several misprints in Eqs. (62), (63) and (64) in Ref. [5]. The collisional contribution to thermal diffusivity has been calculated in both two and three dimensions in Refs. [21, 22]. Because of space limitations, only the leading terms in $1/M$ are given here. For the complete expression, the reader is referred to [22]. To the best of our knowledge, the fluctuation corrections for self-diffusion coefficient are presented here for the first time.

Transport coefficient	Dimension (d)	Kinetic ($k_B T/2$)	Collisional ($a^2/$)
Shear viscosity,	2	$\frac{M}{(M\ 1+e^{-M})\sin^2(/2)}\ 1$	$\frac{1}{6dM}\ M\ \ 1+e^{-M}\ \ [1\ \ \cos(\ )]$
	3	$\frac{5M}{(M\ 1+e^{-M})[2\ \cos(\ )\ \cos(2\ )]}\ 1$	
Thermal diffusivity, D_T	2	$\frac{d}{1\ \cos(\ )}\ \ 1+\frac{2d}{M}\ \ \frac{7\ d}{5}\ \ \frac{1}{4}\csc^2(\ /2)$	$\frac{1}{3(d+2)M}\ \ 1\ \ \frac{1}{M}\ \ [1\ \ \cos(\ )]$
	3		
Diffusion coefficient, D	2	$\frac{dM}{(1\ \cos(\ ))(M\ 1+e^{-M})}\ \ 1$	–
	3		

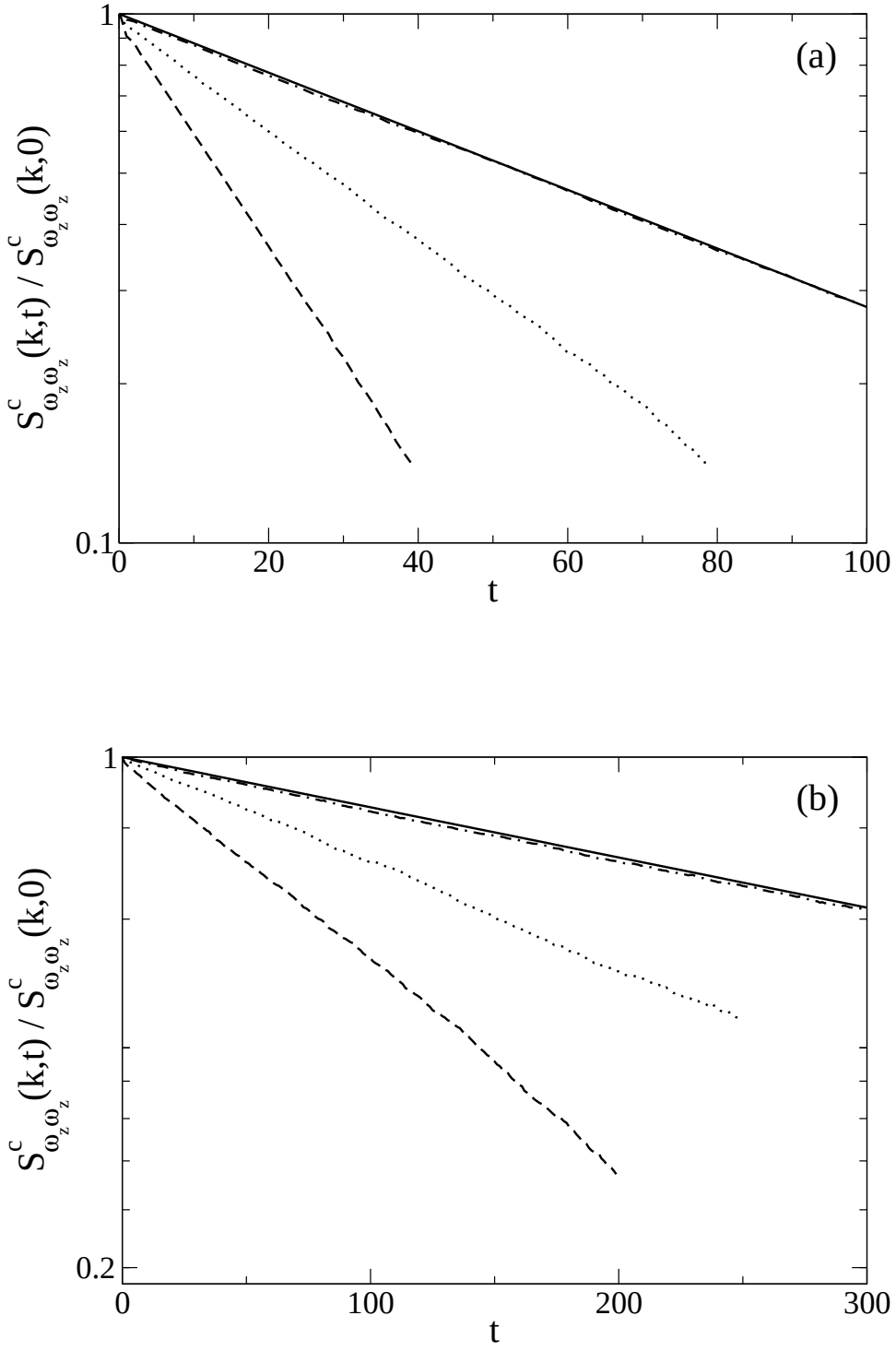

FIG. 1: Normalized vorticity correlations as a function of time for $k = \frac{2}{L}(1;0)$ (dotted-dashed lines), $k = \frac{2}{L}(1;1)$ (dotted lines) and $k = \frac{2}{L}(2;0)$ (dashed lines). The solid line shows Eq. (44) using the theoretical expressions given in Table I for shear viscosity. The decay profiles were fitted to Eq. (44) to obtain values for the shear viscosity . a) $=a = 1:0$, $= 120$, b) $=a = 0:1$, $= 60$. Parameters: $L=a = 32, M = 15$ and $= 1:0$.

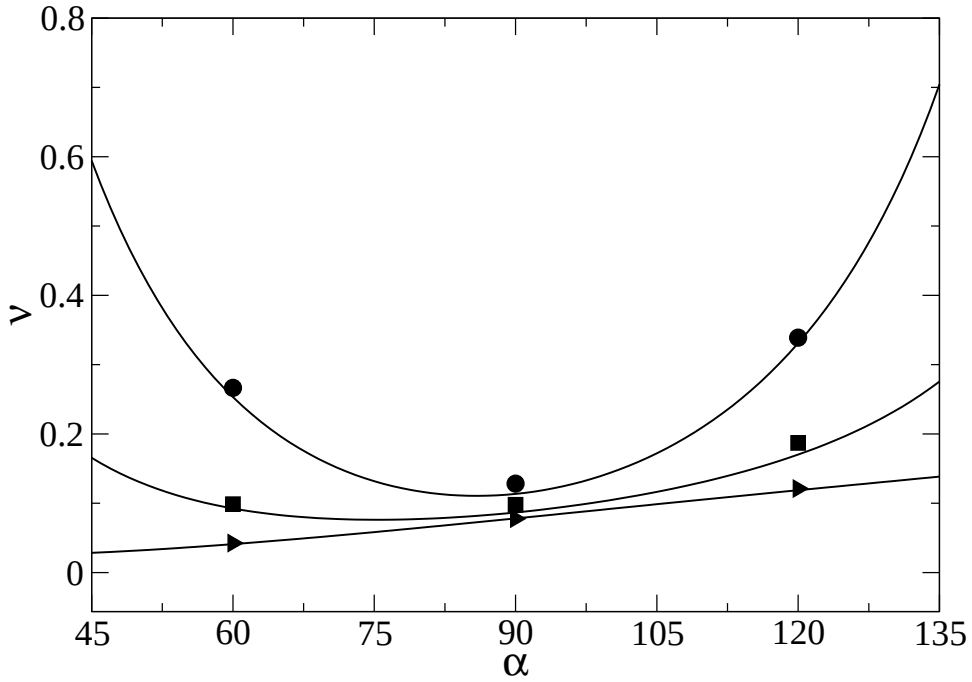

FIG. 2: Shear viscosity as a function of collision angle for mean free paths =a = 0:1 (I);0:5 ( ), and 1:0 ( ) measured using the decay of the vorticity correlations. The solid lines are the theoretical prediction given in Table I, i.e. the sum of the kinetic and collisional contributions. Parameters: L=a = 32, M = 15 and = 1:0.

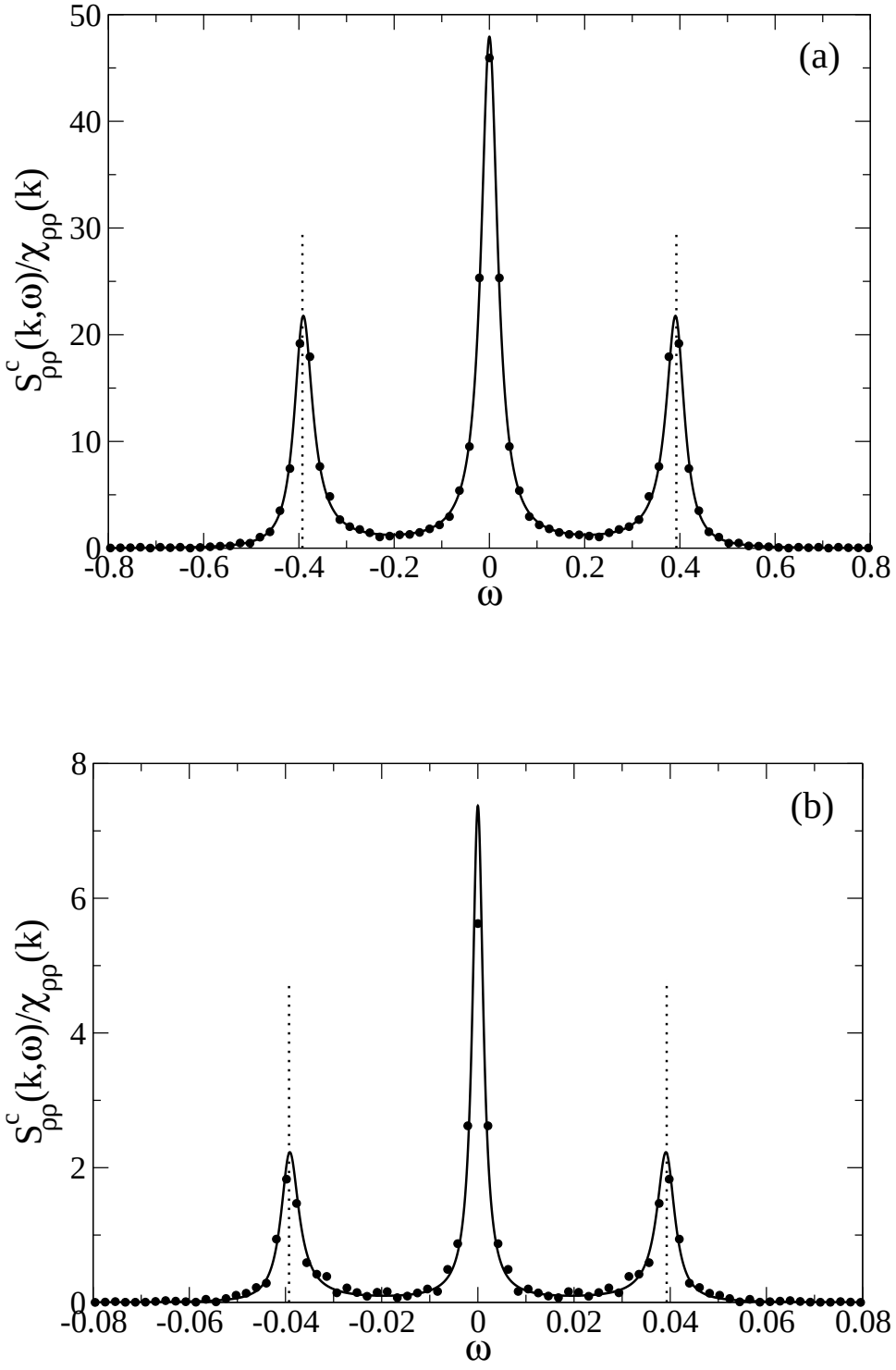

FIG. 3: Normalized dynamic structure factor, $S^c(k;!)= (k)$, for $k = \frac{2}{L}(1;1)$ and a) $=a = 1:0$ with $= 120$, and b) $=a = 0:1$ with $= 60$. The solid line is the theoretical prediction obtained using Eq. (37) and the expressions for the transport coefficients given in Table I. The dotted lines show the predicted positions of the Brillouin peaks using the dispersion relation $! = ck$. Parameters: $L=a = 32, M = 15$ and $= 1:0$.

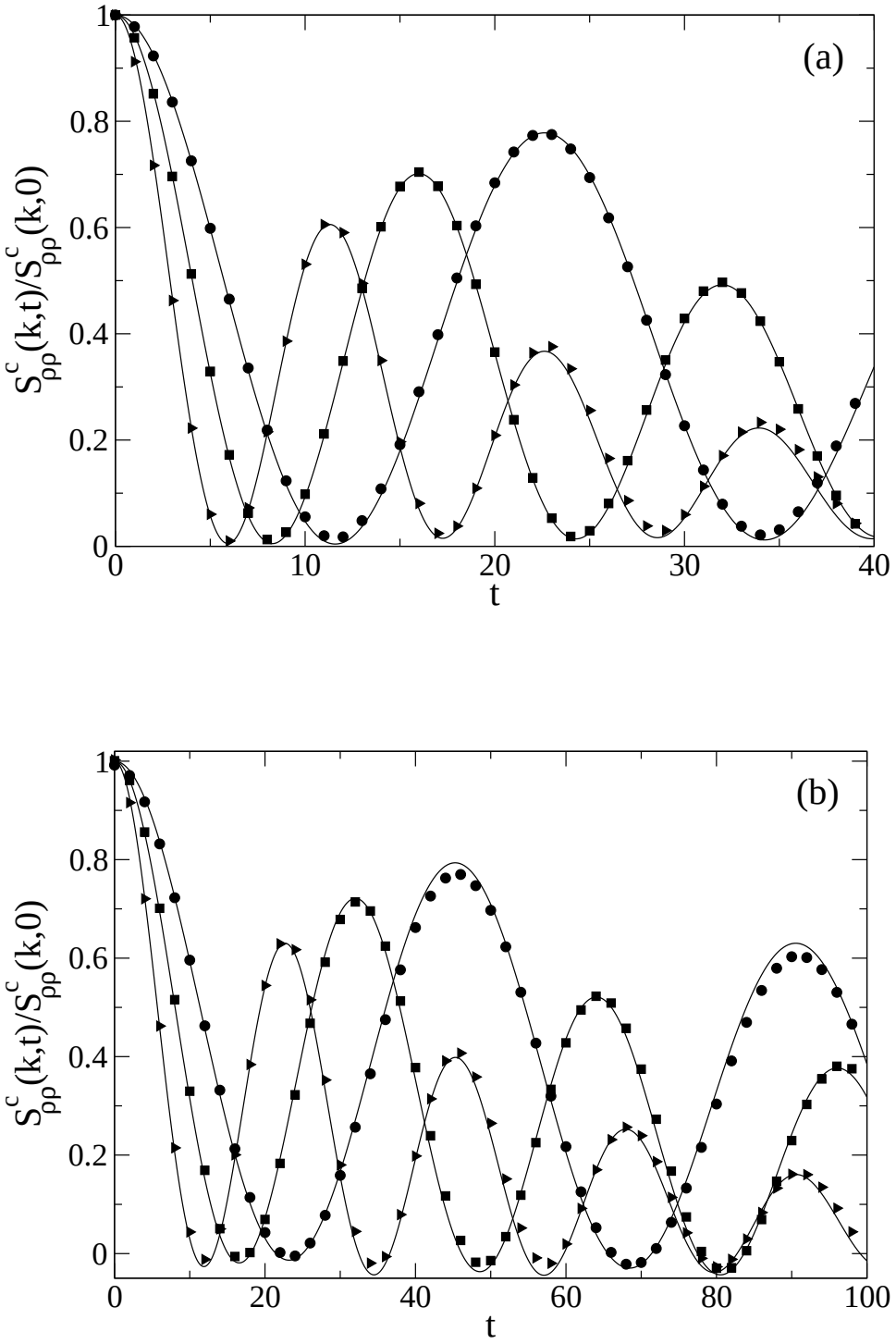

FIG. 4: Normalized density correlations, $S^c(k;t)=S^c(k;0)$, as a function of time, for $k = \frac{2}{L}(1;0)$ ( ), $k = \frac{2}{L}(1;1)$ ( ), and $k = \frac{2}{L}(2;0)$ (I). The solid lines are the theoretical predictions obtained using Eq. (38) and the expressions of transport coefficients given in Table I. a) $=a = 1:0$, $= 120$, and b) $=a = 0:5$, $= 90$. Parameters: $L=a = 32$, $M = 15$ and $= 1:0$.

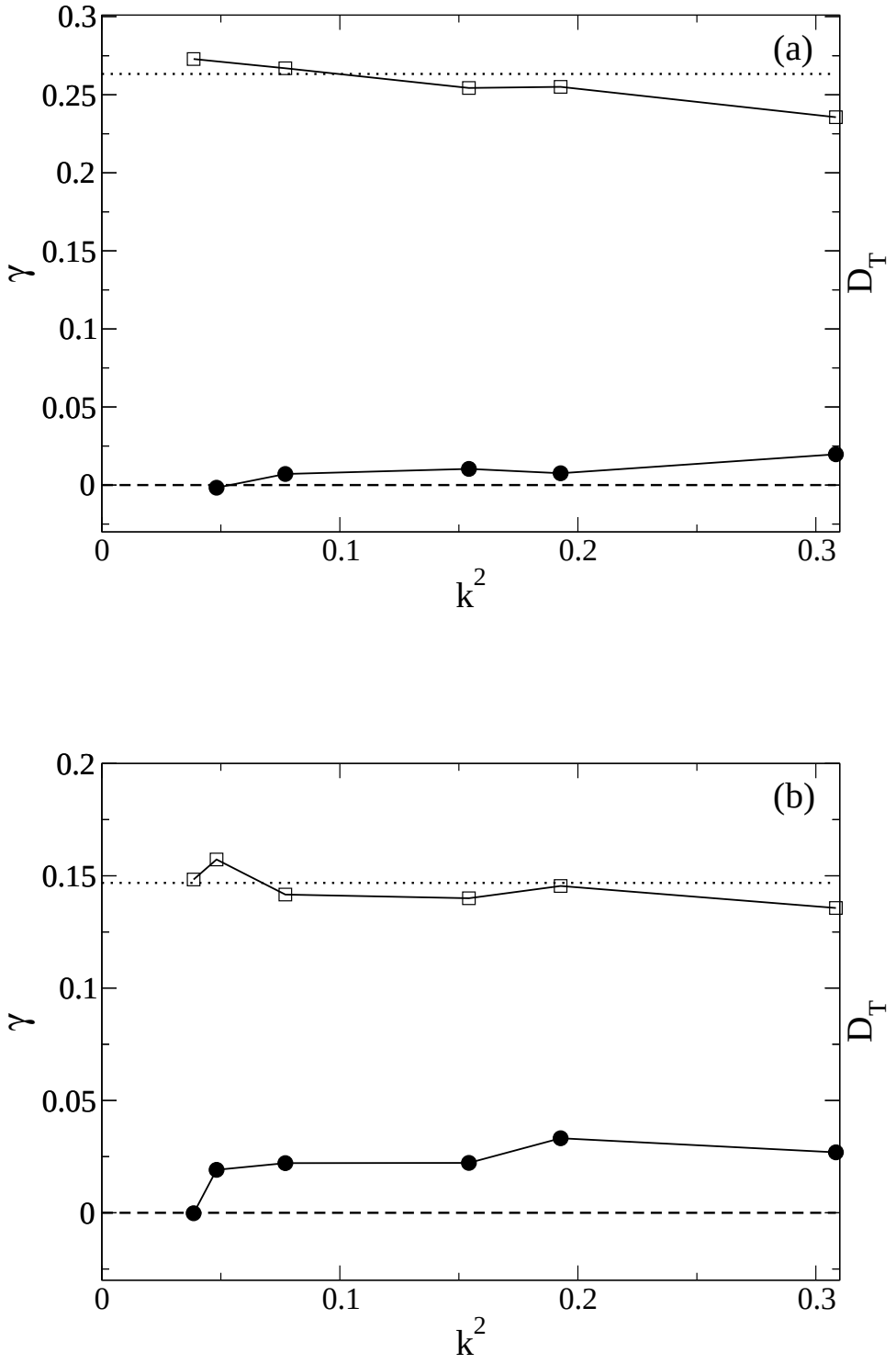

FIG. 5: Fitted values for the bulk viscosity ( ) and thermal diffusivity D_T ( ) as a function of the wave vector squared for a) =a = 1.0 and = 120 , and b) =a = 0.5 and = 90 . Data was obtained by fitting the time dependent density correlations (see Figure 4) using Eq. (38) while keeping D_T and as free parameters. Dashed and dotted lines represent the theoretically predicted values for and D_T, respectively. System size L=a ranges from 32 to 128. Parameters: M = 15 and = 1.0.

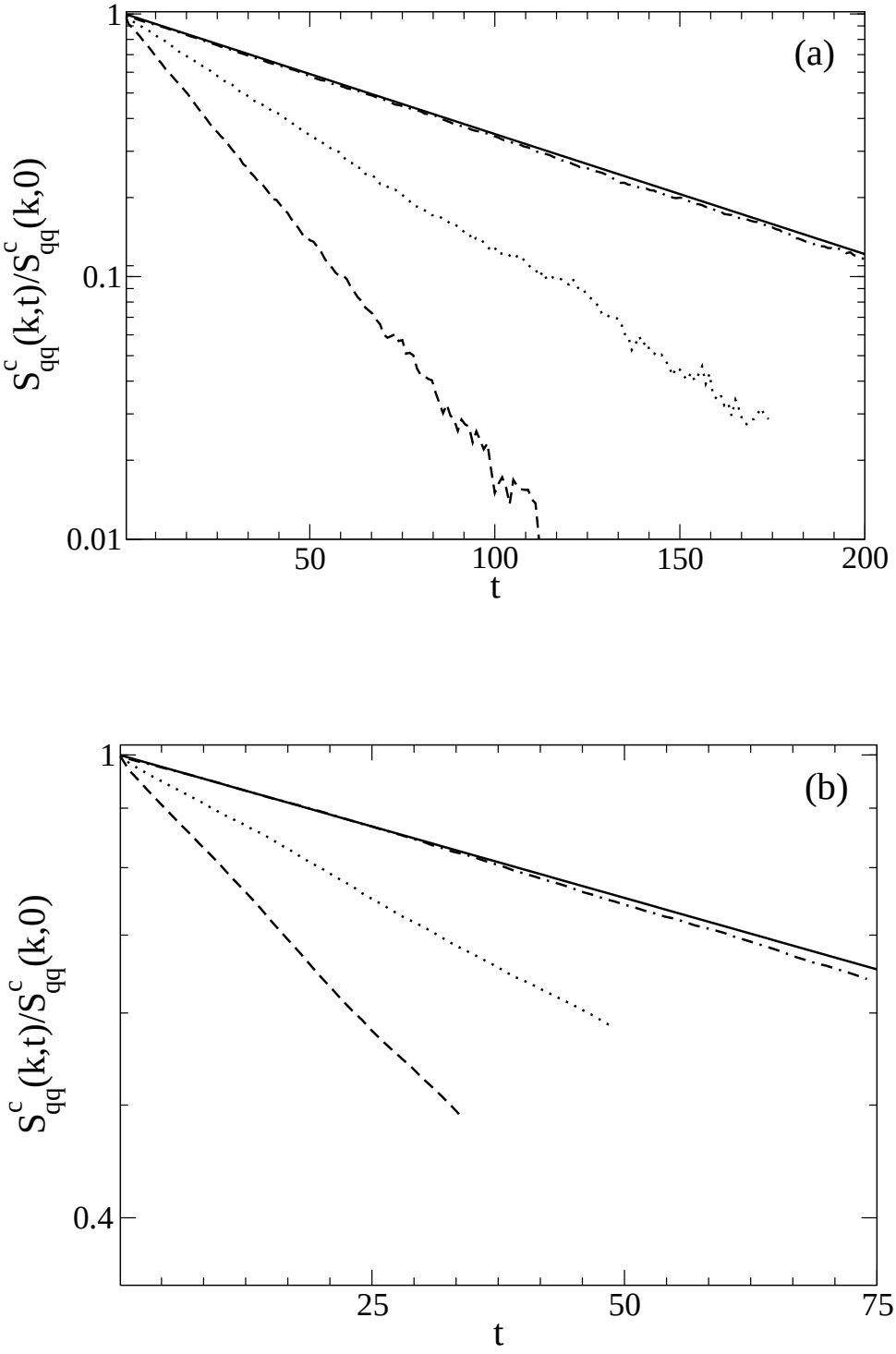

FIG. 6: Normalized entropy correlations, $S^c_{qq}(k;t)=S^c_{qq}(k;0)$, as a function of time for $k = \frac{2}{L}(1;0)$ (dotted-dashed lines), $k = \frac{2}{L}(1;1)$ (dotted lines), and $k = \frac{2}{L}(2;0)$ (dashed lines). The solid line shows Eq. (39) using the theoretical expressions for the thermal diffusivity, D_T, given in Table I. The decay profiles are also fitted to Eq. (39) to obtain unbiased estimates for the thermal diffusivity. a) =a = 1:0, = 120, b) =a = 0:5, = 90. Parameters: L=a = 32, M = 15 and = 1:0.

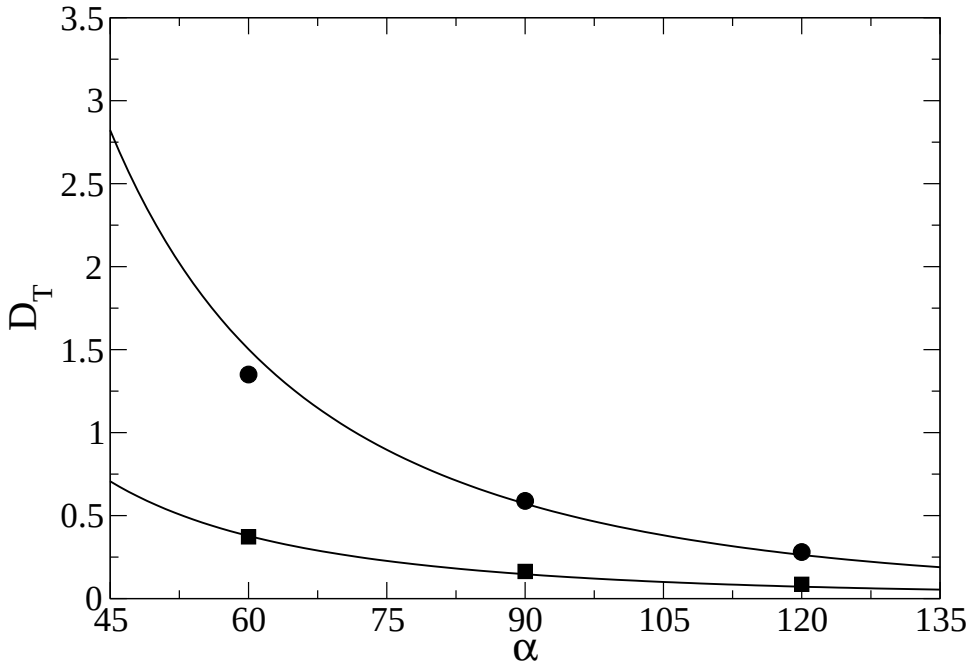

FIG. 7: Estimates for the thermal diffusivity D_T as a function of collision angle for mean free paths $\ell/a = 0.5$ ( ) and 1.0 ( ) obtained by fitting the decay of entropy correlations, $S^c_{qq}(k;t)$. The solid lines are the theoretical prediction given in Table I, i.e. the sum of kinetic and collisional contributions. Parameters: $L/a = 32$, $M = 15$ and $\varepsilon = 1.0$.

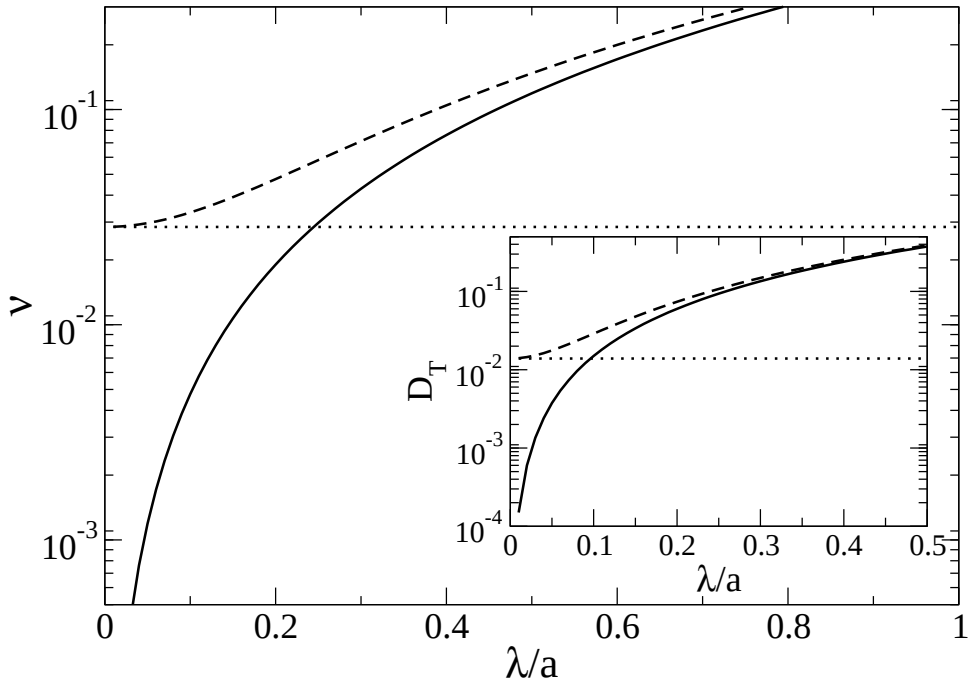

FIG. 8: Shear viscosity and thermal diffusivity D_T (inset) as a function of λ/a. Both plots are obtained using the theoretical expressions given in Table I. The solid and dotted lines are the kinetic and collisional contributions, respectively. The dashed lines are the total contributions to these transport coefficients. For consistency, in the calculation of thermal diffusivity, both the kinetic and collisional contributions are taken only up to and including $O(1/M)$. In the plots, λ/a was varied by changing $k_B T$ for fixed $= 1.0$. Parameters: $M = 3$ and $= 60$.

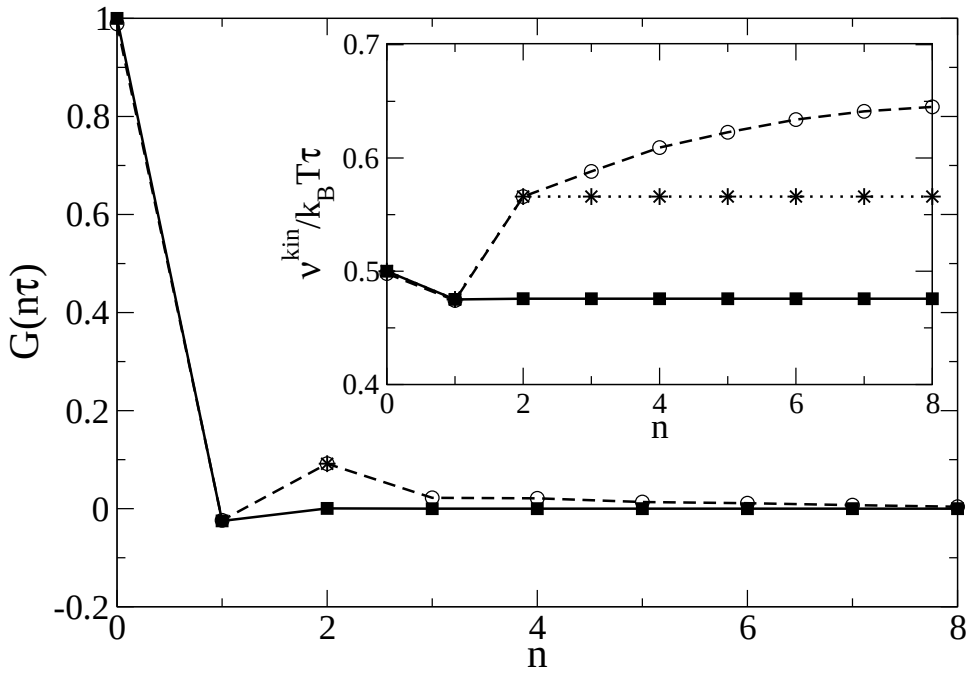

FIG. 9: Stress correlations, $G(n\ )$, as a function of time step n for $=a = 0.25$ and $M = 3$. The inset shows the normalized kinetic contribution to shear viscosity, $^{kin}=k_B T\ $, as a function of time step. The measured values are open circles ( ), and the results of molecular chaos approximation, $G_c(n\ )$ (see Eq. (47)), are filled squares ( ). The asterisk ( ) in the main figure is the prediction of Eq. (63) using the numerically determined values of the probabilities. The asterisks in the inset are a plot of Eq. (65). Parameters: $L=a = 64$, $= 60$, $= 1.0$.

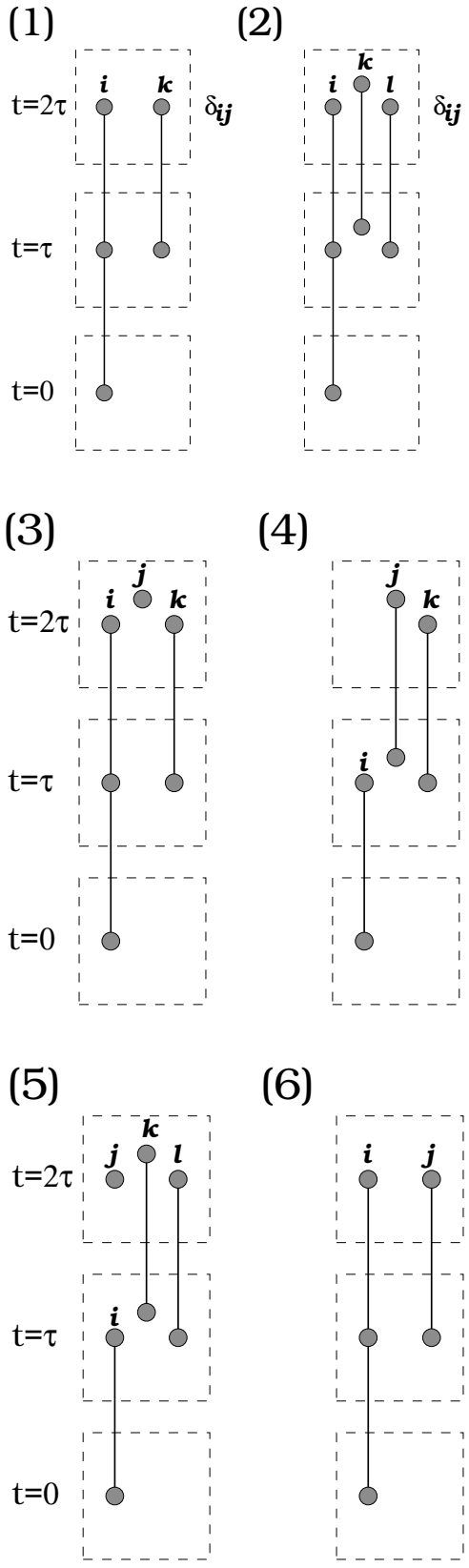

FIG. 10: Diagrams contributing to correlations at $t = 2\tau$ in the calculation of kinetic contributions to shear viscosity. The first two diagrams show the diagonal and the others show the off-diagonal contributions.

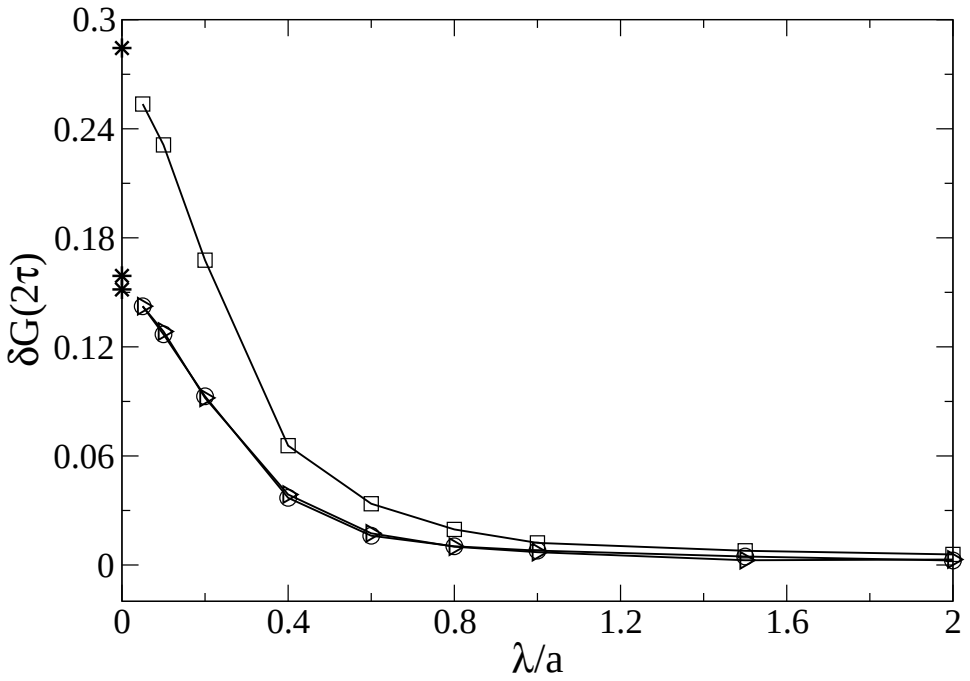

FIG. 11: Correlation contributions $G(2\ )$ as a function of $=a$. Results for collision angles $= 60\ (\ ), 90\ (\ )$, and $120\ (\mathrm{B})$ are presented. The asterisks $(\ )$ are the theoretical predictions in the limit $=a\ !\ 0$. Parameters: $L=a = 64, M = 5, = 1{:}0$.

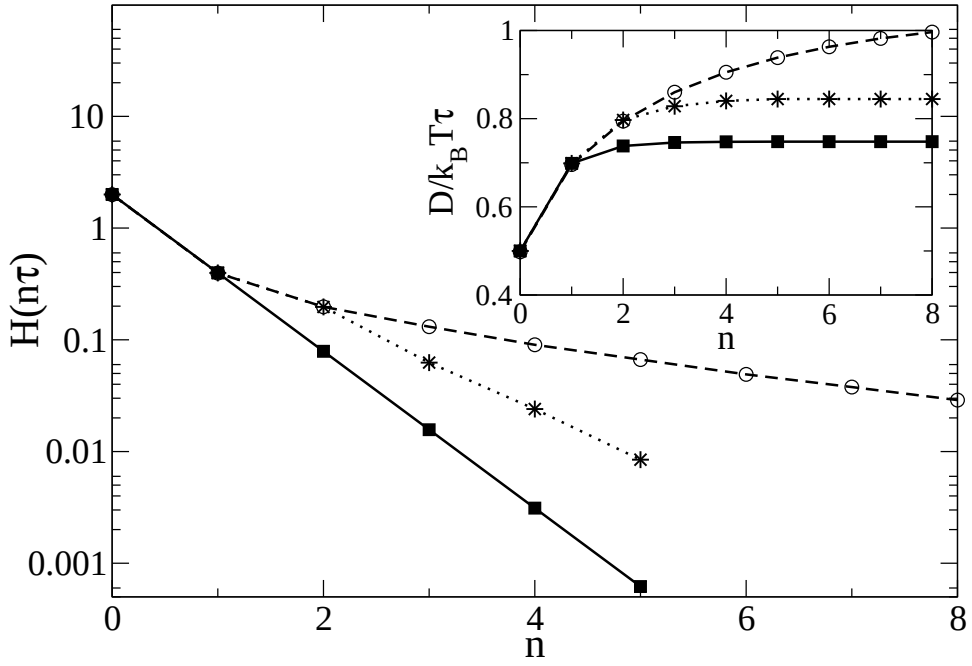

FIG. 12: Normalized velocity auto-correlation function $H(n\ )$ as a function of time step n. Measurement values are shown by open circles ( ), the geometric series by filled squares ( ), and the sum of the geometric series and the correlation contributions (Eq. 72, using the numerically determined p_2) are shown by asterisks ( ). The inset shows the normalized diffusion coefficient, $D=k_B T\ $, as a function of the time step n. The asterisks in the inset are a plot of Eq. (71) using Eq. (72). Parameters: $=a = 0:1$, $= 90$, $L=a = 64$, $M = 5$ and $= 1:0$.

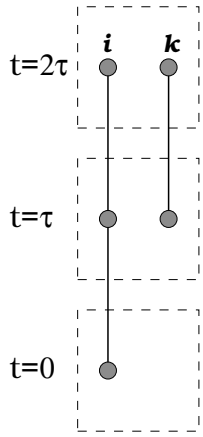

FIG. 13: Schematic diagram showing the configuration contributing to correlations at $t = 2$ in the calculation of self-diffusion coefficient. Particles i and k are in the same shifted collision cell at both $t =$ and $t = 2$. There are M 1 such contributions with probability p_2.

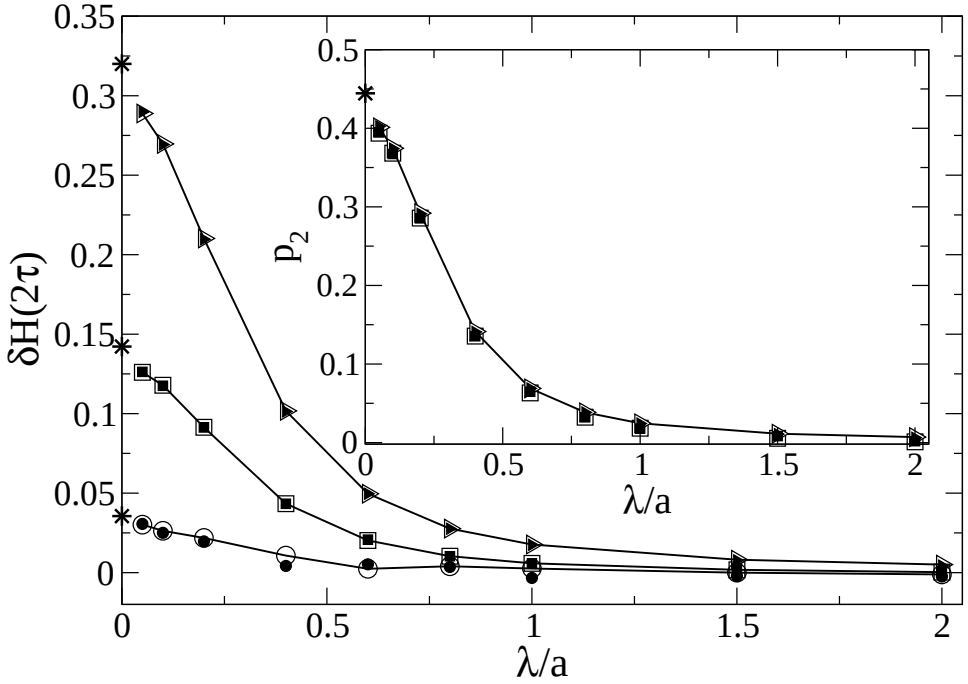

FIG. 14: Correlation contributions at $t = 2$ as a function of λ/a for the self-diffusion coefficient ($\delta H(2\tau)$). Results for collision angles $\theta = 60°$ (▶), 90° (■), and 120° (●) are presented. The open and filled symbols represent data obtained for $\lambda = 1.0$ ($k_B T$ varied) and $k_B T = 1.0$ (λ varied) respectively. The asterisks (*) are the theoretical predictions in the limit $\lambda/a \to 0$. The inset shows the numerically obtained probability p_2 as a function of mean free path for the different parameters considered. Parameters: $L/a = 64$, $M = 5$.

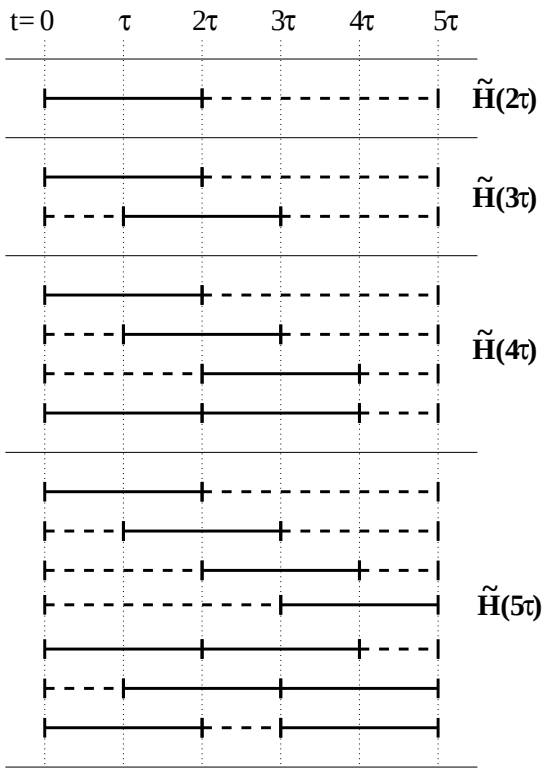

FIG. 15: Schematic diagram of contributions from $\tilde{H}(2\tau)$. Solid lines, all of which have a length of two time steps, show the time span during which particles stay in the same collision cell and are therefore correlated. Dashed lines show the time span in which particles are uncorrelated, so that the molecular chaos assumption is valid. Each solid line will contribute a term $\tilde{H}(2\tau)$ and dashed lines will contribute a factor $H_c(n\tau)$. $\tilde{H}'(n\tau)$ for $n = 2;3;4;5$ show the first four contributions. Note that two consecutive solid lines, i.e. as shown in $\tilde{H}'(4\tau)$, means that particle i is correlated twice for two consecutive time steps, but not with the same particle.

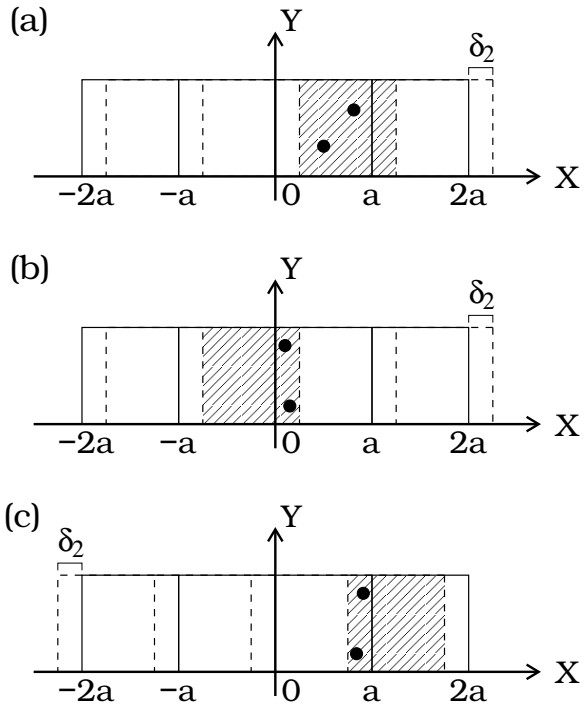

FIG. 16: Schematic diagram showing ways in which two particles can be in the same shifted cell at consecutive time steps. The boxes with solid and dashed borders represent the shifted grids at $t =$ and $t = 2$, respectively. $_2$ is the shift at $t = 2$. The coordinate system uses the shifted frame at $t =$ as a reference. Two particles can be in a) the same shifted cell $_s = 0$ at both $t =$ and $t = 2$, b) cells $_s = 0$ at $t =$ and $_s =$ a at $t = 2$, or c) cells $_s = 0$ at $t =$ and $_s = a$ at $t = 2$. For simplicity, only shifts in x-direction are shown.